ACS APPLIED MATERIALS & INTERFACES

Open Access

This article is licensed under CC-BY 4.0

www.acsami.org

Research Article

Modelling and Emulation of Afferent-Like Excitatory–Inhibitory Spiking Using Ovonic Threshold Devices for Neuromorphic Oscillatory Computing

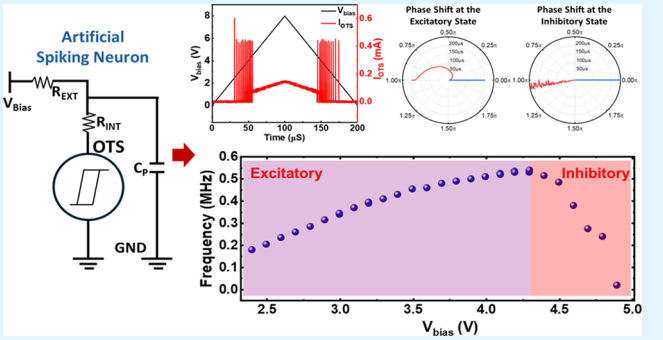
Guosheng Wang,† Zeyu Hu,† Chengcheng Wang, Nishant Saxena, Linxi Zhang, Zheng Chai, Sergey Savel'ev, Alexander Balanov, Pavel Borisov, Fariba Sharifian, Weidong Zhang,* and Muhammad Naqi*

Cite This: *ACS Appl. Mater. Interfaces* 2026, 18, 59518–59533

Read Online

ACCESS | Metrics & More | Article Recommendations | Supporting Information

ABSTRACT: Spike-based computing has attracted increasing attention for efficient information processing, creating demand for neuromorphic hardware capable of generating and processing spikes. Ovonic threshold switching (OTS) devices are promising spiking neurons because their threshold-switching behavior and negative differential resistance enable compact spike-generation circuits, while their scalability supports dense integration. However, a circuit-level design framework linking defect dynamics with conduction behavior remains lacking. Here, we experimentally demonstrate an intensity-tuned artificial neuron based on a GeAsTe OTS device integrated with a resistor-capacitor (RC) circuit. The neuron shows a non-monotonic excitatory–self-inhibitory response with applied voltage, phenomenologically analogous to excitatory–inhibitory behavior in biological neurons. The spiking frequency initially increases and then decreases beyond an inflection voltage point. This transition arises intrinsically from competition between RC charging dynamics and conductive filament retention in the OTS device, rather than from a separate inhibitory pathway. The neuron achieves a spiking frequency of up to 1.6 MHz. The behavior is supported by simulations using a dynamical model for diffusive filament-based memristors, accounting for resistance changes from filament formation and rupture. Furthermore, a physics-informed compact SPICE model combining defect-state transitions and filament evolution reproduces OTS switching and predicts neuron dynamics under varying temperatures, internal resistances, and circuit conditions. Finally, circuit simulations of a coupled OTS neuron network demonstrate vertex coloring with phase convergence within approximately 5 μs, highlighting the potential of this framework for compact, energy-efficient brain-inspired computing.



KEYWORDS: *OTS selector, GeAsTe, artificial spiking neuron, oscillatory neural network, spike-based computing, compact modeling, vertex coloring*

1. INTRODUCTION

In the era of big data and the Internet of Things (IoT), neuromorphic computing has attracted significant attention for its ability to emulate the information-processing mechanisms of the human brain and enable efficient computation for complex tasks such as pattern recognition, object detection, optimization, associative computing, and adaptive control.[1−3] Unlike conventional von Neumann architectures, which physically separate memory and processing units and thus suffer from data transfer bottlenecks, neuromorphic systems integrate information processing and memory, thereby significantly improving energy efficiency and enabling highly parallel data processing.[4−6] Among various neuromorphic computing paradigms, spiking neural networks (SNNs), inspired by biological neuronal communication, have emerged as one of the most promising frameworks for implementing neuromorphic hardware systems due to their event-based computation, in which information is encoded in the timing and/or frequency of spikes rather than continuous-valued signals.[7−10] Such event-based processing allows sparse activity and substantially reduces energy consumption, making spiking neural systems highly attractive for next-generation intelligent systems and edge computing platforms. However, although

Received: July 21, 2026
Revised: October 13, 2026
Accepted: October 13, 2026
Published: October 24, 2026



ACS Publications

© 2026 The Author(s). Published by American Chemical Society

Downloaded from pubs.acs.org/aamick/article-pdf/18/43/59518/6897174/am-2026-15034u.pdf by LIVERPOOL JOHN MOORES UNIV user on 05 November 2026

SNNs are a widely used paradigm in AI with a rich ecosystem of algorithms and software implementations, the range of hardware devices that generate current or voltage spikes remains limited. This motivates the search for a broader and more diverse set of physical realizations of spiking systems.

Spiking neurons are fundamental computational units in SNNs, responsible for integrating incoming signals and generating spike-based outputs that propagate through the network.[7−10] In hardware implementations of SNNs, artificial spiking neurons emulate the temporal dynamics of biological neurons by converting accumulated electrical stimuli or temporal signals into discrete spike signals.[7−10] Complementary metal−oxide−semiconductor (CMOS)-based neuron circuits have been widely explored for emulating neuron-like spiking behavior because of their technological maturity, design flexibility, and compatibility with large-scale integration. Nevertheless, in conventional CMOS implementations, the nonlinear dynamics required for spike generation, such as thresholding, regenerative activation, hysteresis, and adaptation, are generally realized at the circuit level through transistor networks, feedback paths, and capacitive elements. This often leads to rather complex neuron circuits with larger area overhead, which can limit integration density.[11−13] To overcome these limitations, emerging electronic devices with intrinsic nonlinear switching characteristics have been investigated for artificial neuron realization. In particular, nonvolatile memory devices such as phase-change memory (PCM)[14−16] and resistive random-access memory (RRAM)[17−19] have been extensively studied because their resistance modulation under electrical stimulation can emulate the synapse dynamics. However, the nonvolatile switching mechanism of these devices generally requires additional operations to restore the device state, which increases circuit complexity and energy consumption and limits their efficiency for dynamic neuron operations.

To address these challenges, volatile threshold switching (TS) devices have attracted increasing attention for neuron implementations due to their intrinsic nonlinear switching behavior, exhibiting abrupt transitions between high-resistance and low-resistance states, enabling neuron-like integrate-and-fire dynamics when combined with simple passive circuit elements such as resistors and capacitors, and exhibiting a much less noisy response than, for example, diffusive memristors.[13,20] Consequently, TS-based circuits can generate spiking responses without requiring complex reset operations, making them attractive for compact neuromorphic hardware. Several TS materials, including NbO_x and VO_2-based selectors,[21−25] have been explored for neuron implementations. However, device variability and strong parameter dependence in these materials can significantly influence the stability and reliability of the resulting spiking dynamics. Recently, volatile memristors have attracted attention for implementing artificial neurons,[26,27] but they typically either require more complex neuromorphic circuitry or exhibit highly noisy spiking. Neither is optimal for a broad range of applications. In contrast to all the above memristive realizations of artificial neurons, Ovonic Threshold Switching (OTS) devices based on chalcogenide materials offer a very promising alternative and have attracted considerable attention due to their stable switching characteristics, large ON/OFF ratio, and good scalability.[28] In particular, GeAsTe OTS devices offer low switching variability, fast threshold-switching dynamics, and scalability, making them attractive for reliable and high-frequency oscillatory neuron operation.[29,30] When integrated with simple passive circuit elements, OTS devices can reliably generate quite regular neuron-like spiking responses and self-sustained oscillatory dynamics without requiring complex reset circuitry, making them promising building blocks for compact and energy-efficient neuromorphic systems capable of supporting complex brain-inspired computing tasks.[31−33] A GeSe-based OTS neuron has previously demonstrated spike-frequency adaptation (SFA) under a constant bias, a characteristic commonly observed in the mammalian cortex.[32] However, non-monotonic excitatory−inhibitory spiking behavior has not yet been extensively investigated in OTS-based neurons.

Biological neural systems rely on the coordinated interaction of excitatory and inhibitory neurons to regulate information processing and network stability. In particular, non-monotonic neuronal responses, arising from the interplay between excitation and fast, dominant inhibition, enable selective encoding and precise discrimination of input signals.[34−36] Such dynamics give rise to rich oscillatory behaviors, including synchronization and phase segregation, which are closely linked to higher cognitive functions. Inspired by these mechanisms, oscillatory neural networks (ONNs) have emerged as a powerful computational paradigm for solving complex problems such as pattern recognition, graph coloring, and combinatorial optimization, where collective dynamics rather than static states encode information.[2,37]

Herein, we propose a GeAsTe-based ovonic threshold switching (OTS) oscillatory neuron, supported by physics-informed models that establish a direct link between device characteristics and emergent neuronal dynamics. The TiN/GeAsTe/TiN device, fabricated using a 300 mm-compatible process with a 20 nm-thick chalcogenide layer, exhibits low variability (<0.2 V), a high ON/OFF ratio (>10^4), and fast switching speed (∼0.1 ns). Leveraging these properties, a compact resistor−capacitor (RC)-coupled OTS neuron is demonstrated, capable of generating non-monotonic spiking responses under varying stimulus intensities. Through systematic analysis of device and circuit parameters, we first demonstrate that the obtained excitatory−inhibitory dynamics are consistent with the physical mechanism of filament formation and rupture and then propose a threshold-based model, which captures afferent-like excitatory−inhibitory dynamics and accurately predicts diverse spiking behaviors, providing a design framework for scalable neuromorphic circuits. Furthermore, the coupled OTS neuron network exhibits stable phase segregation dynamics that enable the solution of graph coloring problems, independent of excitatory or inhibitory dominance, highlighting the potential of OTS-based oscillatory neurons as compact, energy-efficient building blocks for next-generation brain-inspired computing systems.

2. RESULTS AND DISCUSSION

2.1. Conceptual Framework of Artificial Spiking Neuron Enabled by OTS Device

Figure 1 illustrates the biological inspiration and operating principle of the proposed OTS-based artificial spiking neuron. In biological neural systems, neurons receive synaptic inputs through dendrites, integrate them, and generate action potentials once the membrane potential exceeds a threshold (Figure 1a). These spikes are then transmitted along the axon to downstream neurons and ultimately to higher-order processing regions such as

Downloaded from pubs.acs.org/aamick/article-pdf/18/43/59518/6897117/am-2026-15034u.pdf by LIVERPOOL JOHN MOORES UNIV user on 05 November 2026

https://doi.org/10.1021/acsami.6c15034
ACS Appl. Mater. Interfaces 2026, 18, 59518−59533

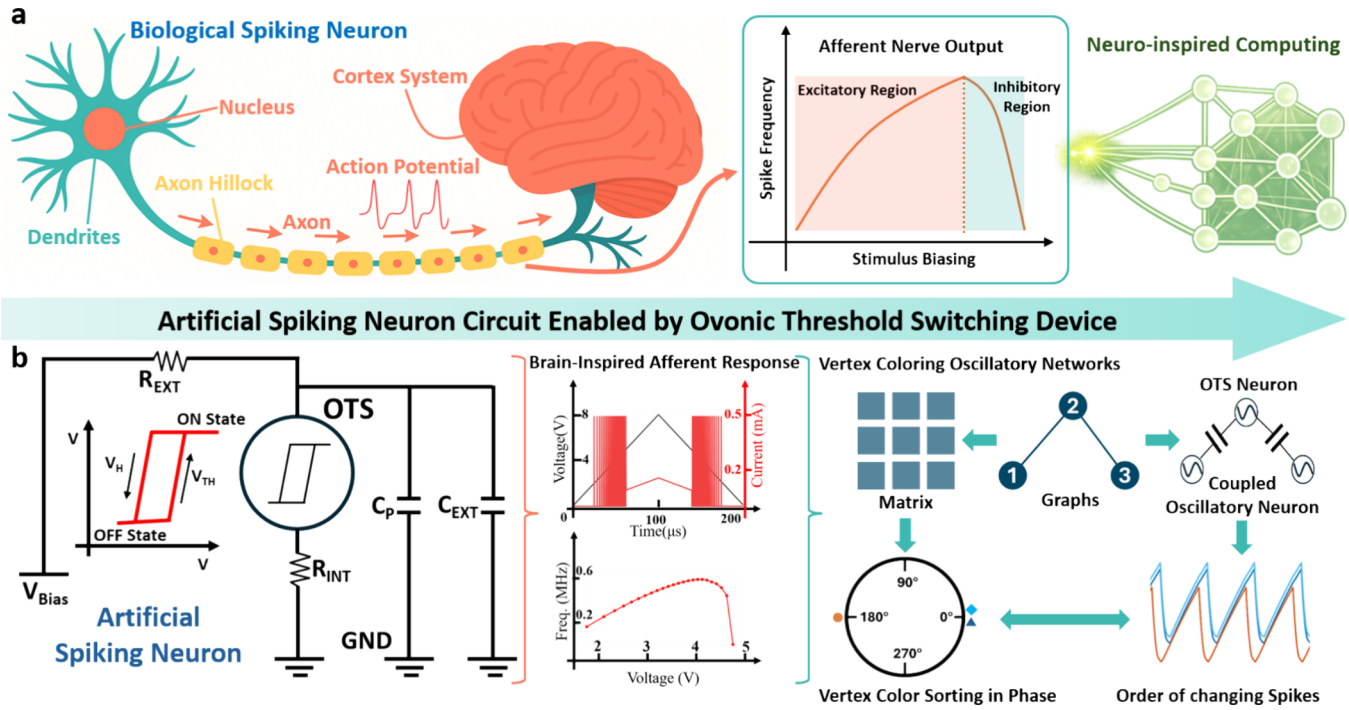


Figure 1. Conceptual layout of biological and artificial spiking neurons. (a) Schematic of a biological spiking neuron illustrating signal integration, action potential generation, and non-monotonic excitatory−inhibitory response. (b) Schematic of an OTS-based artificial neuron circuit generating oscillatory spikes via RC integration and threshold switching, exhibiting excitatory and inhibitory regimes in which information is encoded through spike timing and phase dynamics. The spike frequency shows a non-monotonic dependence on input bias: it initially increases in the excitatory regime and subsequently decreases at higher bias due to prolonged OTS ON-state retention, corresponding to the inhibitory regime. Here, the RC integration is performed by internal device components (internal resistance, R_{int}, and parasitic capacitance, C_p) and external circuit elements (external resistance, R_{ext}, and external capacitance, C_{ext}.

the cortex.[22,38] While many peripheral sensory neurons exhibit monotonic input-output relationships, where firing rate increases with stimulus intensity, more advanced neural circuits, particularly in cortical and sensory processing pathways, often display non-monotonic response characteristics. In such systems, neuronal firing rates initially increase as excitatory drive strengthens with increasing stimulus intensity but decrease when the input becomes excessively strong due to the recruitment of inhibitory or suppressive mechanisms. This excitation−inhibition interplay prevents overexcitation and enables selective sensitivity to specific stimulus ranges.[38−41] The excitatory−inhibitory neural networks proposed by Wilson and Cowan[42] are the key systems for brain computation, allowing analysis of spatially and temporally complex stimuli, e.g., via interference among waves of brain activity.[36,43] Such non-monotonic encoding is particularly advantageous in tasks requiring discrimination of relevant signal ranges rather than simple intensity amplification. Inspired by this principle, we have demonstrated the artificial neuron using a compact circuit consisting of an OTS device, resistive elements, and capacitive components, as shown in Figure 1b. The OTS serves as the core nonlinear element, exhibiting threshold switching and negative differential resistance (NDR) behavior, which enables self-sustained oscillatory spiking behavior. Based on the presented compact OTS circuit, a compact model simulation is performed, where the input voltage is integrated through the RC network until threshold switching triggers spike generation and rapid discharge (Figure 1b). At low to moderate input voltages, the dynamics are dominated by capacitive charging, leading to shorter integration time at higher voltages. As the input increases further, the voltage across the OTS exceeds the holding condition, resulting in prolonged conductive (retention) states and a corresponding decrease in the spiking frequency, referred to here as a self-inhibitory response. The excitatory−inhibitory analogy is phenomenological rather than mechanistic, as this high-bias suppression arises intrinsically from OTS filament retention and the associated increase in holding time, rather than from a separate inhibitory pathway as in biological neural circuits. The competition between RC integration and OTS retention dynamics produces a non-monotonic response: the spike frequency initially increases as the charging time decreases, but at higher bias, the prolonged ON-state holding time broadens the spike duration and increases the oscillation period, resulting in a rapid decrease in spike frequency and eventual suppression of oscillation. The detailed physical mechanism underlying this behavior is further discussed in the following sections. Functionally, the OTS-based neuron can transform analog input signals into frequency-modulated spike trains with selective sensitivity to specific input ranges. As illustrated in Figure 1b, such neurons can be interconnected to form oscillatory networks for neuromorphic computing, where information is represented through spike timing and phase relationships, enabling efficient implementation of constraint-based and optimization tasks, as further demonstrated and discussed in Section 2.7.

2.2. Electrical Characteristics of the OTS Neuron Circuit

To achieve high-performance OTS devices, GeAsTe films were deposited at room temperature using physical vapor deposition (PVD), where TiN was employed as both the top and bottom

https://doi.org/10.1021/acsami.6c15034
ACS Appl. Mater. Interfaces 2026, 18, 59518−59533

Downloaded from pubs.acs.org/aamick/article-pdf/18/43/59518/6897174/am-2026-15034u.pdf by LIVERPOOL JOHN MOORES UNIV user on 05 November 2026

electrodes and deposited in situ with the GeAsTe layer to ensure a clean interface, and the critical dimension of the device, defined by the bottom electrode, ranges from 45 to 150 nm,[29] resulting in a characteristic mushroom-shaped structure as illustrated in the schematic layout of Figure S1a. The electrical characteristics of the OTS device were systematically investigated by applying a triangular voltage pulse (4 V/4 μs), under which the device exhibits typical threshold switching behavior, transitioning abruptly from a high-resistance (OFF) state to a low-resistance (ON) state at the threshold voltage (V_{th}), with a current of ∼0.7 mA at 2 V, and returning to the OFF state when the voltage decreases below the hold voltage (V_h), as shown in Figure S1b. Additionally, DC I-V measurements reveal nonlinear conduction in the OFF state with a current of ∼1.38 × 10^{-8} A at 1 V, consistent with Poole−Frenkel-type transport (Figure S2). Furthermore, cumulative distribution function (CDF) analysis over 2000 switching cycles demonstrates tight distributions of V_{th} and V_h with variations smaller than 0.2 V, confirming excellent device uniformity and reliability (Figure S3). Fast transient measurements under a triangular pulse (4.5 V/1 ns) further reveal ultrafast switching dynamics, with the device turning ON at ∼0.7 ns and a switching time of ∼0.1 ns (Figure S4). The observed phenomenon is complex and has different interconnected mechanisms; thus, we analyze it within three different approaches: (i) a dynamical model describing the evolution of filaments, electron transport, and heat dynamics, (ii) a simpler two-threshold model describing spiking based on a given input of threshold parameters, and (iii) a non-equilibrium kinetic defect model using double-well dynamics. All these approaches provide a diverse and complementary understanding of the observed phenomenon and allow the modeling of potential neuromorphic circuits based on the developed Ovonic spiking elements.

Leveraging the intrinsic threshold-switching characteristics of the GeAsTe-based OTS device, a compact artificial spiking neuron circuit was designed and fabricated, as schematically illustrated in Figure 2a. The circuit consists of an external resistor (R_{ext} = 47 kΩ), an internal resistor (R_{int} = 2.5 kΩ), and a parasitic capacitor (C_p ≈ 117 pF). Here, C_p, originating from the measurement setup, acts analogously to the membrane capacitance of a biological neuron, governing signal integration through the voltage across the OTS (V_{OTS}). To elucidate the neuron dynamics, a triangular voltage input (8 V/100 μs) was applied, and the corresponding oscillatory spiking response was monitored, as shown in Figure 2b,c. Owing to the resistance hierarchy ($R_{int} < R_{ext} \ll R_{off}$), the neuron circuit exhibits three distinct bias-dependent circuit-level operating regimes, denoted R_1−R_3, as shown in Figure 2b. In Region 1 (R_1), the applied bias is too low to drive V_{OTS} to V_{th}, and the OTS remains in the OFF state with only negligible leakage current. As the input bias increases beyond V_{th}, the circuit enters Region 2 (R_2), where repetitive threshold switching gives rise to sustained oscillatory spiking. With a further increase in bias, the neuron transitions into Region 3 (R_3), where the device remains continuously ON and the oscillatory behavior is suppressed. The detailed voltage waveform evolution measured across the OTS in Figure 2c clarifies the physical origin of these three regimes. In R_2, the capacitor charges through R_{ext} until V_{OTS} reaches V_{th}, triggering the abrupt turn-on of the OTS and rapid discharge through R_{int} and the OTS. Once V_{OTS} falls

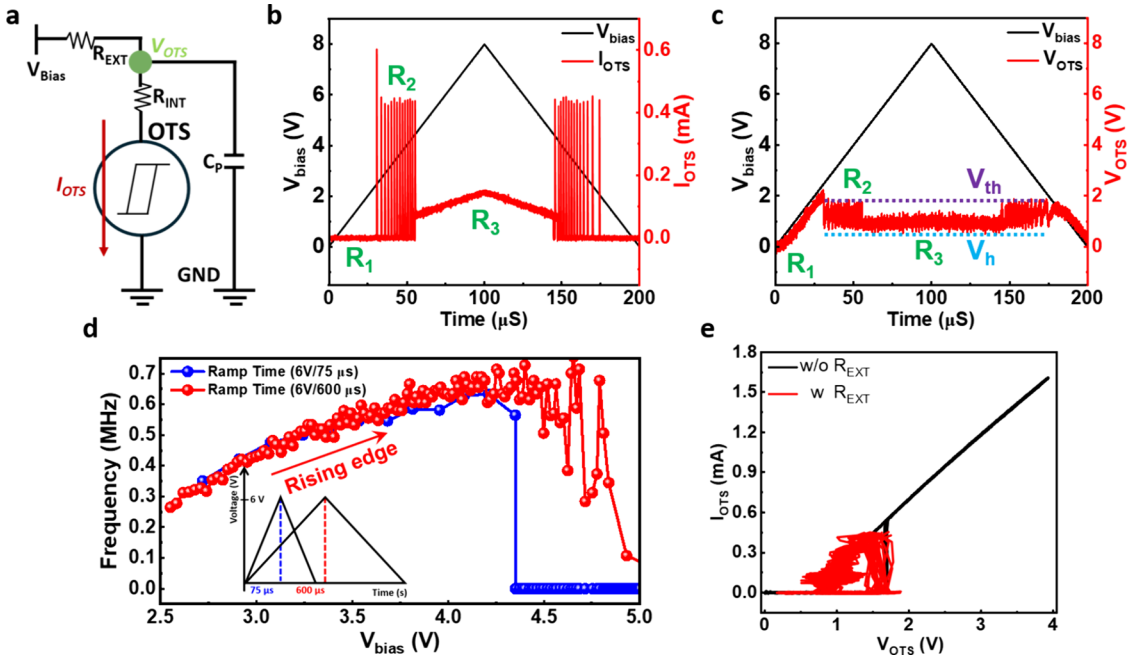


Figure 2. OTS-based artificial spiking neuron and its dynamic response. (a) Schematic of the OTS neuron circuit comprising an external resistor (R_{ext} = 47 kΩ), internal resistor (R_{int} = 2.5 kΩ), and parasitic capacitor (C_p = 117 pF). (b) Temporal response of the neuron under a triangular input bias (8 V/100 μs), showing three circuit-level operational regimes, namely three distinct operational regimes: OFF state (R_1), oscillatory spiking (R_2), and continuously ON state (R_3). (c) Corresponding evolution of V_{OTS}, illustrating switching between threshold voltage (V_{th}) and hold voltage (V_h) in the spiking regime. (d) Frequency as a function of input bias extracted from the rising edges of triangular inputs with ramp rates of 6 V/75 μs and 6 V/600 μs (inset showing ramp setting). The slower ramp rate provides more time for OTS relaxation and more clearly resolves the high-bias frequency-suppression region before oscillation terminates. (e) Comparison of the V_{OTS}−I_{OTS}characteristics between the neuron circuit (with R_{ext}) and the standalone OTS device (without R_{ext}). The circuit preserves the intrinsic threshold switching dynamics of the OTS device.

https://doi.org/10.1021/acsami.6c15034
ACS Appl. Mater. Interfaces 2026, 18, 59518−59533

Downloaded from pubs.acs.org/aamick/article-pdf/18/43/59518/6897174/am-2026-15034u.pdf by LIVERPOOL JOHN MOORES UNIV user on 05 November 2026

below V_h, the conductive filament collapses (as demonstrated by the own filament base model above), switching the device back to the OFF state and initiating the next charging cycle. This repeated charge−discharge process produces periodic spiking, with V_{OTS} oscillating between V_h and V_{th}. Notably, the first spike exhibits a higher V_{th}, which can be attributed to the longer relaxation time before the initial firing event. At sufficiently high bias in R_3, V_{OTS} remains above V_h even after discharge, preventing filament rupture and thereby maintaining the OTS in a continuously ON state. Under this condition, the device no longer switches off, and spiking is suppressed, corresponding to an inhibitory-like response governed by the combined influence of filament stability and circuit dynamics. In addition, a temporal delay of approximately 5 μs between the applied bias (V_{Bias}) and V_{OTS} is observed in Figure 2c, arising from the RC charging process determined by R_{ext} and C_p.

To quantify the relationship between input intensity and neuronal response, the spike frequency was calculated as $f = 1/\Delta t$, where Δt is the inter-spike interval between two consecutive OTS switching-current peaks. An enlarged view of the rising-edge waveform in Figure 2b is provided in Figure S5a to illustrate the frequency-extraction procedure. Figure 2d presents the frequency−bias responses extracted from the rising edges of triangular inputs with ramp rates of 6 V/75 μs and 6 V/600 μs. The slower ramp rate provides more time for OTS relaxation during the increasing-bias sweep, allowing the high-bias frequency-suppression region to be resolved more clearly before oscillation terminates. The corresponding time-domain response for the slower ramp rate of 6 V/600 μs is further shown in Figure S5b. Near the inflection point and the upper oscillation boundary, frequency extraction from the continuously varying triangular input becomes more sensitive because the inter-spike interval increases and fewer switching events are available. Therefore, the frequency response and its statistical reproducibility were further evaluated under stepwise constant-bias conditions, as discussed in Section 2.5. As the input bias increases, the firing frequency initially rises, indicating excitatory behavior, and reaches a maximum at approximately 4.1 V. Beyond this point, the frequency rapidly decreases, signifying a transition to an inhibitory regime. To elucidate the origin of this inhibitory behavior, the spike waveforms at representative biases of 2.8 and 4.3 V were analyzed, as shown in Figure S6a,b, respectively. At the lower bias of 2.8 V, corresponding to the excitatory regime, the neuron exhibits sharp and narrow spikes with a short discharge duration. In contrast, at the higher bias of 4.3 V, the spike becomes significantly broader, indicating that the device remains in the ON state for an extended period after discharge. The effective discharge and retention interval is defined as T_h, representing the duration over which the OTS remains conductive before returning to the OFF state. This behavior arises because, at higher bias (near Region 3), the post-discharge voltage across the OTS remains close to or above V_h, preventing immediate filament rupture and delaying the off process. As a result, the effective spiking rate decreases, leading to inhibitory behavior. To assess the reproducibility of the frequency−voltage response, both cycle-to-cycle (C2C) and device-to-device (D2D) variations were evaluated, as shown in Figure S7a,b, respectively. The C2C analysis was performed over 20 repeated cycles, whereas the D2D analysis was performed across five independently measured OTS neuron devices. The mean spike frequency and standard deviation were determined as a function of applied bias. The C2C variation remains relatively small over most of the oscillatory range but increases near the high-bias transition. The D2D variation is larger, particularly near this transition, because device-to-device differences in the switching and holding characteristics shift the bias at which the frequency begins to decrease.

To further examine the influence of peripheral circuit elements, the intrinsic OTS characteristics were compared by extracting V_{OTS}−I_{OTS} trajectories and benchmarking them against the standalone I−V characteristics without R_{ext}, as shown in Figure 2e. The close agreement between the two confirms that the fundamental switching dynamics of the OTS are preserved within the circuit and that the external resistor primarily introduces temporal delay rather than altering the intrinsic device behavior, validating the use of device-level models for circuit-level design and optimization.

2.3. Numerical Modeling of the OTS-Based Artificial Neuron

To gain insight into the occurrence of spiking and the nonmonotonic dependence of the spiking rate on the applied voltage observed experimentally, we adopted the model previously used to identify self-sustained spiking modes in diffusive memristors[26] for numerical simulations; see Section 4 for details. The model predicts both the onset and termination of spiking, as shown in Figure 3a (blue spiking curve), which are governed by two threshold voltages. No spiking occurs below the lower threshold. Consistent with the experimental observations, above this threshold, the inter-spike interval initially decreases, reaches a minimum, and then increases again until spiking abruptly ceases at the upper threshold.

Figure 3b clearly shows this behavior, which enables the artificial neuron's excitatory−inhibitory response, by plotting the spiking rate as a function of the externally applied voltage. The rate was calculated by extracting the inter-spike intervals from panel (a) and taking their inverse, following the standard procedure used in biological spike-train analysis, as was also done for the experimental measurements.

To uncover the instabilities leading to the onset and termination of self-sustained spiking, we conducted a bifurcation analysis of the different dynamical regimes with variations in the external voltage. Figure 3a (red, green, dashed black, and orange lines) and Figure 3c illustrate the bifurcation structure calculated using numerical continuation with the AUTO routines integrated into XPPAUT software.[44,45] Panel (a) displays the complete bifurcation diagram, including the stable and unstable fixed-point and limit-cycle branches. Panel (c) offers an enlarged view of the region near the Hopf bifurcation (HP), detailing the unstable limit-cycle branch and suggesting its connection to the stable oscillatory solution through period-doubling bifurcations of limit cycles ($PD_{1,2}$).

The analysis indicates an Andronov−Hopf instability associated with both self-sustained oscillation thresholds. This mechanism is supported by the finite spiking rate observed at the threshold voltages. Numerical simulations (Figure 3a, blue curve) further reveal that the non-monotonic evolution of the spiking rate is governed by the phenomenological electrochemical potential near the filament tip, a characteristic feature of filamentary devices.

2.4. Compact Model for the Ovonic Threshold Switch

While the dynamical model captures the filamentary physical origin of the excitatory−inhibitory behavior qualitatively, its inherent complexity makes a quantitative description of the

Downloaded from pubs.acs.org/aamick/article-pdf/18/43/59518/6897174/am-2026-15034u.pdf by LIVERPOOL JOHN MOORES UNIV user on 05 November 2026

https://doi.org/10.1021/acsami.6c15034
ACS Appl. Mater. Interfaces 2026, 18, 59518−59533

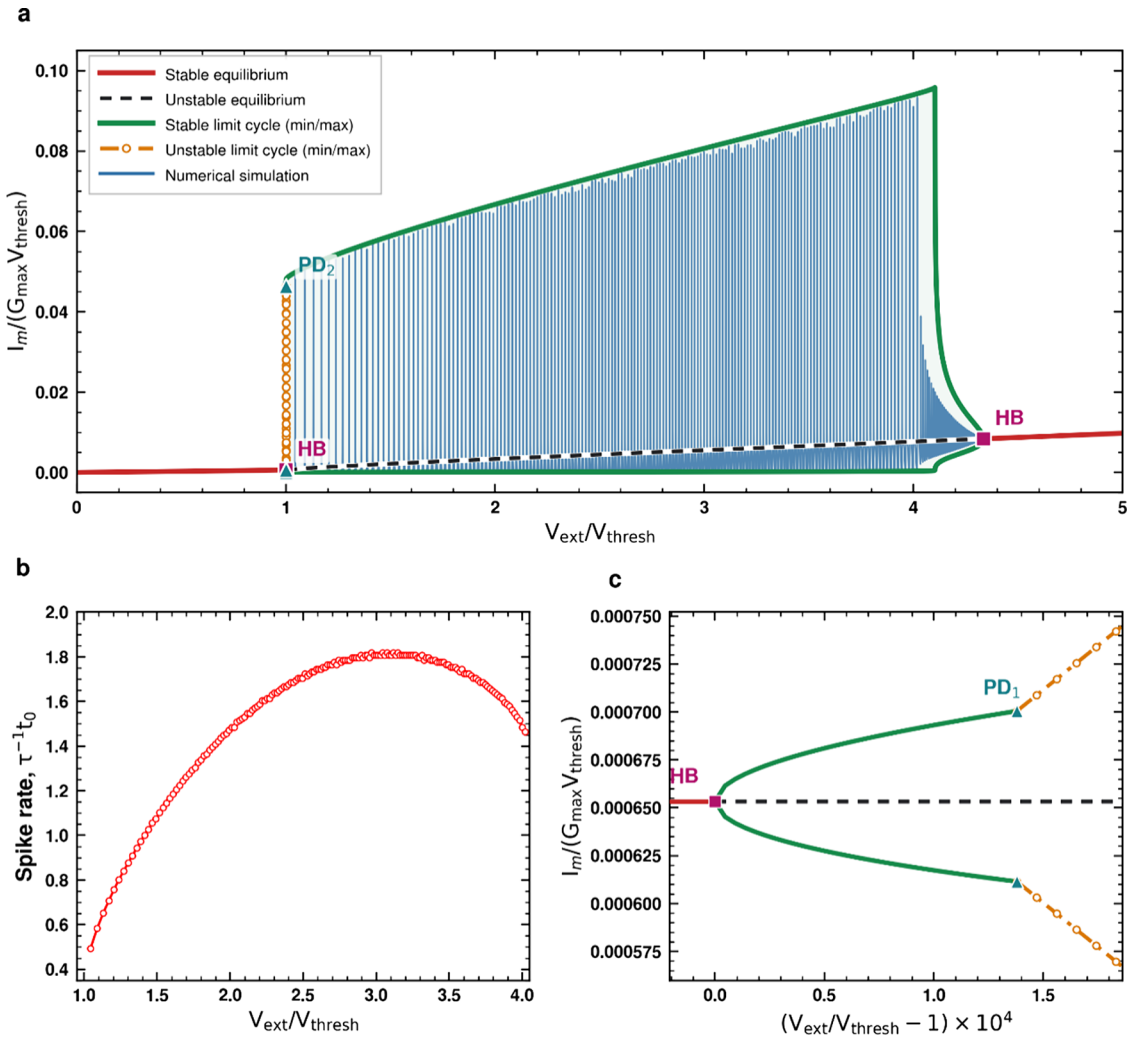


Figure 3. Simulated bifurcation-driven spiking dynamics of the artificial memristive model. (a) A bifurcation diagram illustrating the appearance and disappearance of self-oscillations, including a stable equilibrium (red curve), unstable equilibrium (black dashed curve), stable limit cycle with min and max values of oscillating currents (green curve), and unstable limit cycle with min and max (orange curve with open circle). Inside the green limit cycle, simulations of eqs 1a−1e are presented: normalized current ($I_m/G_{max}V_{thesh}$) as a function of normalized external voltage (V_{ext}/V_{thesh}), showing the onset and termination of self-sustained spiking between lower and upper threshold voltages. (b) Normalized spiking rate extracted from the inter-spike intervals in panel (a) and plotted as a function of normalized voltage. The spiking rate initially increases with voltage, reaches a maximum, and then decreases before the abrupt disappearance of oscillations. (c) A zoomed-in part of the bifurcation diagram in (a). HB and $PD_{1,2}$ denote the onset of Andronov-Hopf and period-doubling bifurcations, respectively.

experimental measurements challenging. This complexity arises from electron tunnelling through the filaments, heat transport, and the dependence of heat generation on the filament structure. As a result, the model requires the definition of numerous parameters, including the electrochemical potential, which are not readily accessible experimentally. To date, a unified compact model that simultaneously captures defect dynamics and electrical $I-V$ characteristics of OTS devices for circuit-level design remains limited.[20,28,46] Here, we propose a physics-based compact model, which does not require the pre-assumed knowledge of the evolution of filaments. Instead, it combines double-well defect kinetics with an effective, averaged description of filament behavior, rather than explicitly modelling its full dynamics,[22] enabling accurate reproduction of both OTS switching behavior and neuron-like spiking. The experimental and simulated results are shown in Figure 4a, where the single OTS device is characterized under a triangular voltage pulse (4 V/4 μs), with Stages 1−4 representing its device-level evolution during one complete voltage sweep. The proposed model successfully reproduces the characteristic $I-V$ curve, including the threshold switching and hysteresis. Based on the voltage-sweep direction and current evolution, the switching process is divided into four distinct stages, with corresponding physical states illustrated in Figure 4c. In this representation, green circles denote delocalized defects, whereas red circles represent localized defects. The microscopic mechanism is governed by the double-well defect energy model shown in Figure 4b, where each defect can exist in either a localized or delocalized state. According to the distributed Poole−Frenkel (DPF) model,[47] defects in different states exhibit different resistances. The resistance of a delocalized defect is assumed to be R_0, while the resistance of a localized defect is given by $R_{loc} = R_0 \exp\left(\frac{E_a}{kT}\right)$, where k is the Boltzmann constant, and T is the temperature. The activation energy E_a is determined by the

https://doi.org/10.1021/acsami.6c15034
ACS Appl. Mater. Interfaces 2026, 18, 59518−59533

Downloaded from pubs.acs.org/aamick/article-pdf/18/43/59518/6897174/am-2026-15034u.pdf by LIVERPOOL JOHN MOORES UNIV user on 05 November 2026

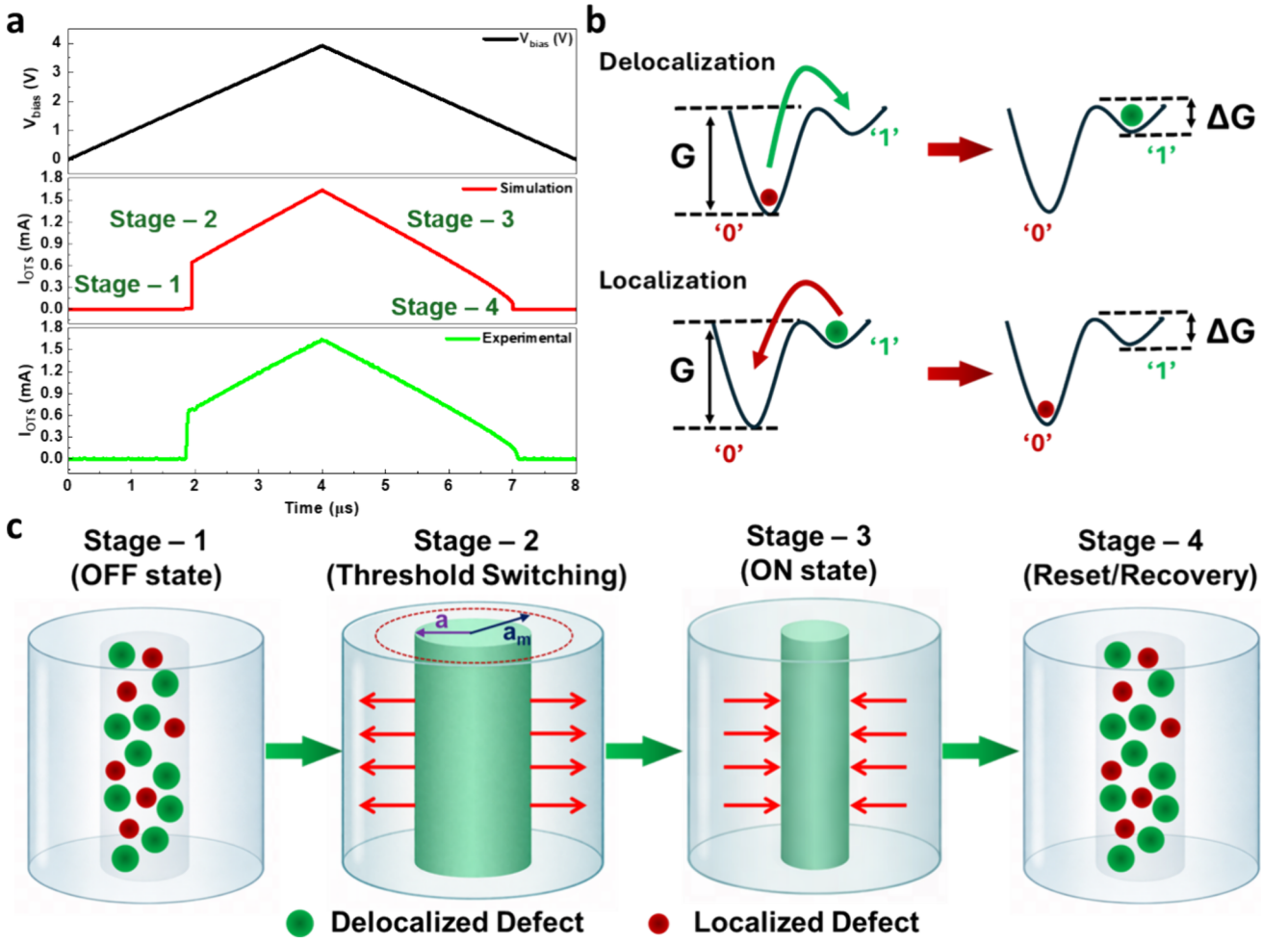


Figure 4. Compact modeling framework of the OTS device. (a) Experimental and simulated I–V characteristics of the GeAsTe-based OTS device under a triangular voltage pulse, indicating the threshold switching behavior and its division into four stages during the voltage sweep: Stage 1, OFF-state leakage conduction; Stage 2, filament increasing after switching on; Stage 3, ON-state conduction during the decreasing voltage sweep; and Stage 4, return to the OFF state at V_h. (b) Schematic of the double-well defect energy model, showing transitions between localized ("0") and delocalized ("1") states driven by the electric field and Joule heating. (c) Physical evolution of the conductive path during threshold switching. Red and green spheres represent localized and delocalized defects, respectively. Under an increasing electric field, defect delocalization and radial expansion of the conductive filament occur, increasing the filament radius from a to a_m. During relaxation, the conductive path shrinks, and defects return to the localized state, resulting in recovery of the OFF state.

difference between the conduction band and the Fermi level and is reduced by the applied electric field F, expressed as $E_a = E_c - E_f - \alpha F$, where $E_c$is the conduction band energy, $E_f$is the Fermi level, and α represents the field coupling factor. Due to this exponential dependence, localized defects exhibit significantly higher resistance than delocalized defects. To simplify the transport model, the conductive path is approximated as a cylindrical channel. During Stages 1 and 4 (OFF state), the current mainly flows through paths dominated by localized defects, resulting in high resistance and limited conduction. The transition between localized and delocalized defect states governs both the off-state current and the switching process.[48−50] The defect dynamics are described using the double-well model, where the localized state ('0') has a higher energy barrier G, and the delocalized state ('1') has a lower energy barrier ΔG, as illustrated in Figure 4b. The transition between these states is driven by both the electric field and Joule heating (IV), which effectively lowers the energy barrier and facilitates defect activation. The transition kinetics are characterized by two time constants. The time constant for the transition from the localized to the delocalized state is given by $\tau_{01} = \exp\left(\frac{G - s\cdot IV - b\cdot F}{kT}\right)$, where s and b represent the sensitivity to electrical power and electric field, respectively. Similarly, the reverse transition time constant from the delocalized to the localized state is $\tau_{10} = \exp\left(\frac{\Delta G}{kT}\right)$. Based on these phenomenological, thermodynamical transition rates, the evolution of the number of delocalized defects (n) along the conduction path can be described as $\frac{dn}{dt} = \frac{N-n}{\tau_{01}} - \frac{n}{\tau_{10}}$ where N is the total number of defects. As the applied bias increases, the number of delocalized defects increases progressively until they form a continuous conductive filament bridging the electrodes, which corresponds to the threshold switching (ON state). Once the filament is formed, the OTS switches to a low-resistance state, and the voltage across the device drops. The high current flowing through the filament generates significant Joule heating, which stabilizes the conductive path and maintains the ON state. In this regime, the device can be approximated as a resistor with low resistance.

Downloaded from pubs.acs.org/aamick/article-pdf/18/43/59518/6897174/am-2026-15034u.pdf by LIVERPOOL JOHN MOORES UNIV user on 05 November 2026

https://doi.org/10.1021/acsami.6c15034
ACS Appl. Mater. Interfaces 2026, 18, 59518−59533

To capture the nearly constant voltage drop in the ON state, the filament is modeled with a bias-dependent radius a, with a maximum radius a_m. The evolution of the filament radius is governed by the competition between thermal expansion and relaxation, described by $\frac{da}{dt} = (a_m - a)\, c \cdot IV - \frac{a}{t_d}$, where c is the sensitivity to Joule heating and t_d is the filament shrinkage time constant. During the rising edge of the voltage, the filament radius increases due to increasing power, while during the falling edge, the filament shrinks as the power decreases, leading to the off process. Finally, the proposed model successfully captures the influence of temperature and internal resistance (R_{int}) on device characteristics, as validated in Figures S8 and S9, respectively. With increasing temperature, the activation energy is reduced, resulting in a lower threshold voltage V_{th}, while the holding voltage V_h remains relatively unchanged (Figure S8). The close agreement between experimental data and simulation confirms that the model accurately captures the thermally activated switching behavior. In contrast, increasing the internal resistance R_{int} reduces the current flowing through the device and suppresses Joule heating, thereby making defect activation more difficult. As a result, the defects remaining in the off state and the filament radius decrease, leading to both the threshold voltage V_{th} and holding voltage V_h increasing simultaneously with increasing R_{int} (Figure S9). The model quantitatively reproduces this trend and shows strong agreement with experimental observations across a wide resistance range, thus demonstrating that the proposed model not only captures the intrinsic switching mechanism but also reliably predicts the impact of external circuit parameters, confirming its suitability for accurate device−circuit co-design.

To further evaluate the physical roles of the key parameters in the compact model, we investigated the dependence of the switching characteristics on G, ΔG, E_a, N, and the filament shrinkage time constant t_d, as shown in Figure S10. The parameters G and E_a have pronounced effects on the threshold voltage V_{th}, whereas ΔG provides a comparatively moderate modulation of V_{th}. The holding voltage V_h remains relatively insensitive to these parameters over the investigated ranges. In contrast, the total number of defects N mainly influences V_h and the ON-state current. Increasing N increases the effective resistance of the conductive path, resulting in a reduced ON-state current and an increased V_h, while V_{th} remains nearly unchanged. The filament shrinkage time constant t_d governs filament relaxation; a smaller t_d leads to faster filament shrinkage, making the conductive state more difficult to establish and sustain. The variable n, representing the number of delocalized defects, evolves dynamically according to the defect-transition kinetics and is therefore not treated as an independently adjustable model parameter. Together, these results clarify how the key physical parameters govern OTS switching and provide a basis for analyzing the excitatory-inhibitory spiking dynamics discussed in the following section.

2.5. Analysis of excitatory−Inhibitory Spiking Using the Proposed OTS Neuron Circuit

To further investigate the oscillator dynamics, a stepwise DC bias was applied to the artificial spiking neuron with a duration of 200 μs per step. The resulting spike frequency as a function of bias is presented in Figure 5a, exhibiting a pronounced nonmonotonic dependence with a maximum at ∼4.3 V; the neuron operates in the excitatory regime, where increasing bias enhances the firing frequency. Beyond this transition, further increases in bias lead to a gradual suppression of oscillations, and the frequency eventually drops to zero at ∼5 V, where the OTS remains in a stable ON state. Compared with measurements under triangular excitation (Figure 2b), the extended duration at each bias provides sufficient time for filament evolution and rupture, thereby revealing a more prominent inhibitory regime. In addition, the corresponding current responses across different biases (2.4−4.8 V, 0.6 V step size) reveal the clear evolution of switching dynamics, as shown in Figure 5b. To further evaluate the temporal stability of the neuron under constant-bias operation, the period jitter was analyzed from consecutive inter-spike intervals (ISIs), as shown in Figure S11. At a fixed bias of 2.46 V, the ISI remains narrowly distributed around approximately 3.2−3.4 μs, with a standard deviation of approximately 0.1 μs and an overall variation below approximately 0.7 μs. These results demonstrate stable spike timing in the regular oscillatory regime. The timing variation becomes larger toward the high-bias inhibitory regime, consistent with the increasing influence of stochastic filament-retention and rupture dynamics. The coexistence of excitatory and inhibitory behaviors can be understood through load-line analysis within the negative differential resistance (NDR) region, as illustrated in Figure 5c. Oscillations occur only when the load line intersects the NDR region; otherwise, the device remains either permanently OFF (low bias) or ON (high bias), consistent with the behavior shown in Figure 2b. Within the oscillatory regime, increasing bias shifts the load-line intersection toward the holding current (I_h) region. At sufficiently high bias, the operating point approaches a condition where the device voltage (V_{OTS}) is slightly higher than V_h, leading to a quasi-stable ON state and stochastic behavior of filament rupture. As the bias increases, the filament becomes stronger and more stable, reducing the probability of spontaneous rupture and significantly increasing the T_h.[51,52] Although similar firing frequencies are observed at low (2.4 V) and high (4.8 V) biases, their underlying mechanisms differ fundamentally, as demonstrated by the representative spike waveforms in Figure 5d,e, respectively. In the excitatory regime (2.4 V), the current exhibits two-state switching, characterized by a relatively long charging time (τ_c) and short holding time. In contrast, in the inhibitory regime (4.8 V), a distinct three-state current behavior emerges, where prolonged T_h coexists with shorter charging times. The observed longer waiting time between several closely located spikes can be understood via thermal barrier hopping in the double-well potential of the kinetic model. Despite this difference in current dynamics, V_{OTS} consistently exhibits bistable transitions governed by capacitor charging and discharging. In the inhibitory regime, V_{OTS} stabilizes near V_h, and the current remains close to the holding current prior to filament rupture. This extended ON-state dwell time gives rise to the observed three-state current behavior and results in a reduced oscillation frequency. It is necessary to point out that, at higher bias, the OTS neuron should not be interpreted as a uniformly slowed regular oscillator in which every inter-spike interval progressively increases. Instead, the experimental response becomes increasingly stochastic because of the stochastic nature of intrinsic conductive-filament retention and rupture. Relatively short inter-spike intervals can therefore be interrupted by occasional prolonged conductive-state intervals, which increase at higher bias and in turn increase the average oscillation period and reduce the average firing frequency. This behavior is directly

Downloaded from pubs.acs.org/aamick/article-pdf/18/43/59518/6897117/4/am-2026-15034u.pdf by LIVERPOOL JOHN MOORES UNIV user on 05 November 2026

https://doi.org/10.1021/acsami.6c15034
ACS Appl. Mater. Interfaces 2026, 18, 59518−59533

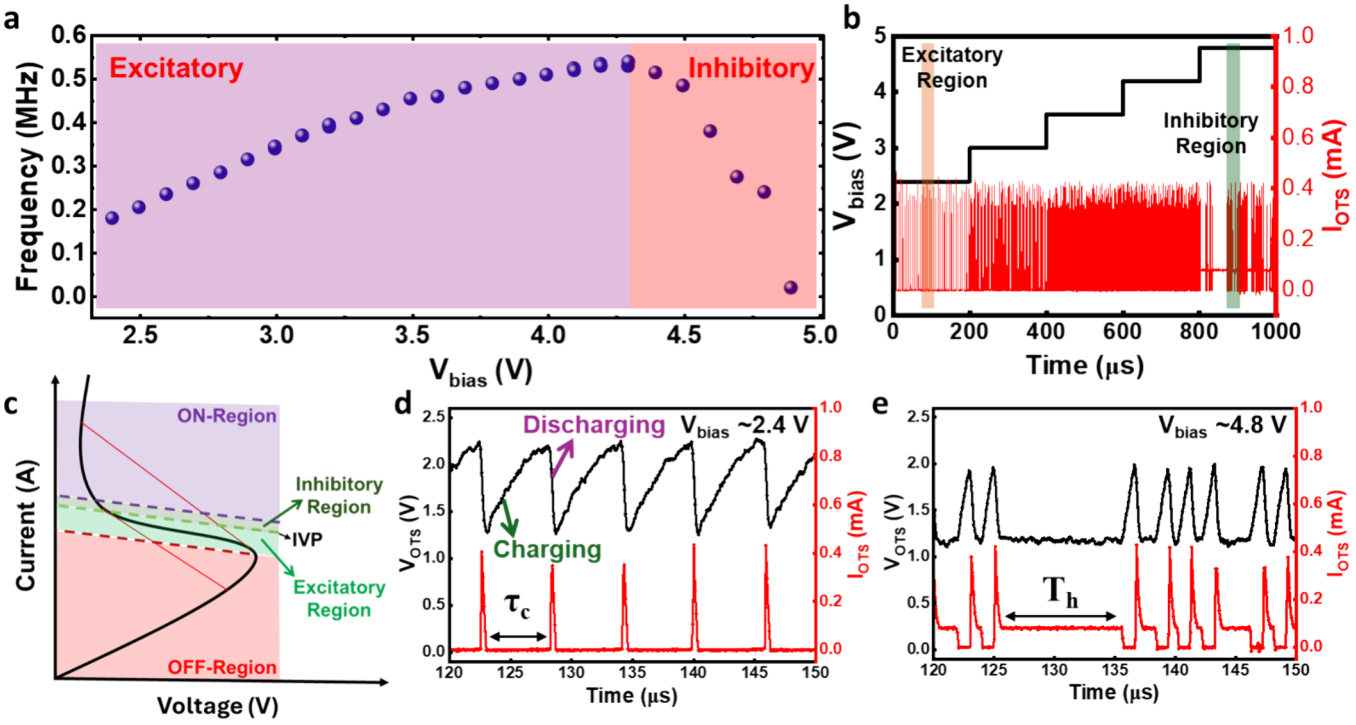


Figure 5. Analysis of excitatory−inhibitory spiking dynamics. (a) Spike frequency as a function of applied bias, indicating a non-monotonic response with an inflection voltage point near 4.3 V, which separates the excitatory and inhibitory regimes. (b) Time-domain current responses of the OTS-based artificial neuron under different biases from 2.4 to 4.8 V. (c) Load-line analysis in the NDR region illustrating the transition from excitatory to inhibitory operation. In the excitatory region, the load-line intersects the OTS curve below the holding current, enabling rapid switching and recovery. In the inhibitory region, the cross-point shifts close to or above the holding current, resulting in prolonged retention of the ON state. (d,e) Representative spike waveforms in the excitatory regime at 2.4 V and the inhibitory regime at 4.8 V, respectively. At low bias, the neuron exhibits sharp and narrow spikes with short holding time. At high bias, the waveform becomes broader because of the increased retention interval (T_h), leading to a reduction in spike frequency.

supported by the additional temporal analysis presented in Figure S12. To quantify the bias-dependent temporal dynamics, each oscillation cycle was separated into the charging time τ_c, discharging time τ_d, and retention time τ_r, with the holding time defined as $T_h = \tau_d + \tau_r$, as shown in Figure S12a. The statistical analysis shows that τ_c generally decreases with increasing bias, whereas prolonged retention events become increasingly prominent in the high-bias regime. Near the frequency-turnover voltage, extended retention remains limited, while at higher bias the retention-time distribution broadens substantially. These opposing trends confirm that the non-monotonic frequency response under constant-bias operation arises from the competition between faster charging and increasingly prolonged conductive-state retention. To examine the influence of the frequency-extraction method, the firing frequency was calculated using both the inverse of the mean inter-spike interval (ISI) and the inverse of the median ISI, as shown in Figure S13. Both methods exhibit very similar frequency-voltage characteristics and preserve the same non-monotonic trend. At higher bias, the median-based frequency is slightly higher because it is less sensitive to occasional long ISIs associated with stochastic filament retention. The evolution of the characteristic time constants further clarifies this mechanism: T_h increases gradually in the excitatory regime but rises more rapidly in the inhibitory regime, while τ_c decreases with increasing bias, as shown in Figure S14, exhibiting opposite trends. The shapes of the current spikes and voltage charging−discharging cycles in both excitatory and inhibitory regimes are well described by the dynamical model, as shown in Figure S15. To quantitatively capture this competition, the gradients of τ_c and T_h with respect to bias were analyzed (Figure S16). The sum of these gradients approaches zero at ~4.3 V, corresponding to the inflection voltage point (IVP) in spike frequency, given by $R_{ext} \cdot I_h + V_h$, indicating a dynamic balance between RC charging (driving oscillation) and filament retention (suppressing switching) that governs the transition from excitatory to inhibitory behavior. The energy consumption per spike was further investigated under different R_{int}, R_{ext}, and C_{ext} conditions, as summarized in Figure S17 of the Supporting Information. For R_{int} = 10, 2.5, and 600 Ω, minimum energies of approximately 0.16, 0.15, and 0.13 nJ/spike are obtained (Figure S17a), respectively, with corresponding maximum firing frequencies of approximately 220 kHz, 600 kHz, and 1.6 MHz. Variation of R_{ext} and C_{ext} also modifies the energy−voltage characteristics and the accessible oscillatory range, demonstrating that the energy consumption can be tuned through the external circuit parameters (Figure S17b,c, respectively). Relatively low sub-nJ energy consumption is maintained during regular excitatory oscillation, whereas the energy per spike increases at higher bias as prolonged OTS ON-state retention increases the conductive duration while suppressing the firing frequency. A comparison with representative OTS- and memristor-based artificial neurons is provided in Table S1.

https://doi.org/10.1021/acsami.6c15034
ACS Appl. Mater. Interfaces 2026, 18, 59518−59533

Downloaded from pubs.acs.org/aamick/article-pdf/18/43/59518/6897174/am-2026-15034u.pdf by LIVERPOOL JOHN MOORES UNIV user on 05 November 2026

2.6. Influence of External Circuit Parameters on OTS Neuron Dynamics

To further evaluate the impact of external circuit parameters on the oscillatory behavior of the OTS-based neuron, the spike frequency is jointly governed by the interplay between external resistance (R_{ext}), external capacitance (C_{ext}), and internal resistance (R_{int}), each contributing differently to the charging and retention dynamics of the device, as shown in Figure 6a–c, respectively. For varying R_{ext}, the peak oscillation frequency remains nearly unchanged, indicating that the upper frequency limit is primarily determined by intrinsic device switching dynamics (Figure 6a) (location between two Hop bifurcations). However, at a given bias, increasing R_{ext} reduces the spike frequency in the comparable excitatory region due to prolonged RC charging time, as evidenced by the systematic increase in τ_c (Figure S18a). In contrast, the T_h remains largely unaffected by R_{ext}, since the discharge process is dominated by the intrinsic pathway through C_p and R_{int}, rather than the external resistor (Figure S18b). Consequently, increasing R_{ext} shifts the IVP toward higher bias, as maintaining the OTS voltage near V_h requires a larger applied bias to drop across the external resistance at a certain current, thereby delaying the transition from excitatory to inhibitory behavior. Furthermore, the effect of C_{ext} was investigated by introducing an external capacitance in parallel with C_p (Figure 6b), resulting in a reduction of the maximum oscillation frequency due to the increased charging and discharging times, consistent with the trends observed in τ_c and T_h in Figure S19a,b, respectively. Despite this temporal modulation, the IVP remains largely unchanged, as the capacitance modifies the circuit time constants without significantly altering the voltage distribution across the OTS device, thereby preserving the condition for sustaining $V_{OTS} \approx V_h$. Next, the influence of R_{int} was investigated, as shown in Figure 6c. Increasing R_{int} leads to a pronounced reduction in maximum frequency and accelerates the transition into the inhibitory regime. At low bias, R_{int} has a negligible effect on frequency, as it does not significantly impact the charging time (Figure S20a). However, it strongly modulates the T_h (Figure S20b), which becomes dominant at higher bias and governs the suppression of oscillations. Physically, a smaller R_{int} results in higher holding current (I_h) and lower V_h. As mentioned above, the IVP is mainly controlled by I_h and R_{ext}; hence, smaller R_{int} leads to a higher IVP. Additionally, normalized frequency-voltage characteristics were analyzed to elucidate the origin of the observed behavior, revealing that the non-monotonic excitatory–inhibitory transition is an intrinsic property of the OTS switching dynamics, independent of variations in R_{ext}, C_{ext}, and R_{int}, as shown in Figure S2a–c, respectively. While the external resistive and capacitive elements modulate the temporal response by tuning the charging and discharging times, they do not alter the underlying mechanism governing the transition. Instead, these circuit parameters primarily induce a horizontal, vertical, or scaled shift in the response, while preserving the overall shape of the frequency profile. In addition, the R_{ext}, R_{int}, and C_{ext}-dependent frequency responses were evaluated across three devices (Figure S22), confirming that the characteristic circuit-parameter-dependent trends are preserved despite device-to-device variations.

2.7. Vertex Coloring Using Oscillatory OTS Neuron Networks

To demonstrate the potential of the OTS neuron in neuromorphic computing, a 3-node oscillatory neural network is simulated using the compact OTS model to solve the vertex colouring problem. This problem is a non-deterministic polynomial-time hard (NP-hard) combinatorial optimization problem, in which adjacent vertices in a graph must be assigned different colors using the minimum number of colors.[2] Conventional digital approaches suffer from exponentially increasing computational cost with graph size, making real-time or energy-efficient solutions challenging.[53] Neuromorphic oscillatory networks provide a promising alternative by naturally encoding solutions in their phase dynamics.[54,55] Based on the excitatory-inhibitory dynamics established in our OTS neuron system, we further extend this framework to implement a coupled oscillatory network for solving the vertex coloring problem, as illustrated in Figure 7a. The presented excitatory-inhibitory behavior provides a tunable mechanism for controlling both the temporal evolution and relative phase ordering of individual neurons, allowing each neuron to encode graph constraints into physical dynamics. In the proposed network, each vertex is represented by an OTS-based oscillatory neuron, while edges between vertices are implemented through coupled capacitors. Each OTS neuron is modeled using $R_{int} = 2.5$ kΩ, $R_{ext} = 47$ kΩ, and $C_p = 117$ pF. The graph edges are implemented through coupling capacitors of $C_c = 2$ pF between connected neurons, producing phase-repulsive interactions. Initially, all three nodes exhibit nearly identical oscillatory waveforms and can therefore be regarded as occupying the same phase state (same color). As the coupled dynamics evolve,

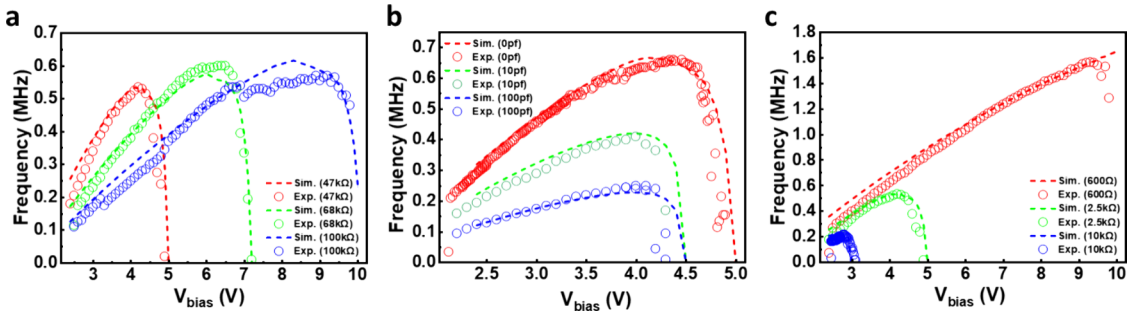


Figure 6. Influence of circuit parameters on the oscillatory dynamics of the OTS neuron. Spike frequency as a function of bias voltage under varying circuit parameters. (a) Effect of external resistance, $R_{ext} = 47$, 68, and 100 kΩ. Increasing R_{ext} prolongs the RC charging time and shifts the inflection voltage point to a higher bias. (b) Effect of external capacitance, $C_{ext} = 0$, 10, and 100 pF. Increasing capacitance prolongs both the charging and discharging processes, leading to a reduction in the maximum spike frequency. (c) Effect of internal resistance, $R_{int} = 600$, 2.5, and 10 kΩ. Increasing R_{int} reduces the OTS current, resulting in a shift of the operating region toward lower bias and lower spike frequency.

https://doi.org/10.1021/acsami.6c15034
ACS Appl. Mater. Interfaces 2026, 18, 59518–59533

Downloaded from pubs.acs.org/aamick/article-pdf/18/43/59518/6897174/am-2026-15034u.pdf by LIVERPOOL JOHN MOORES UNIV user on 05 November 2026

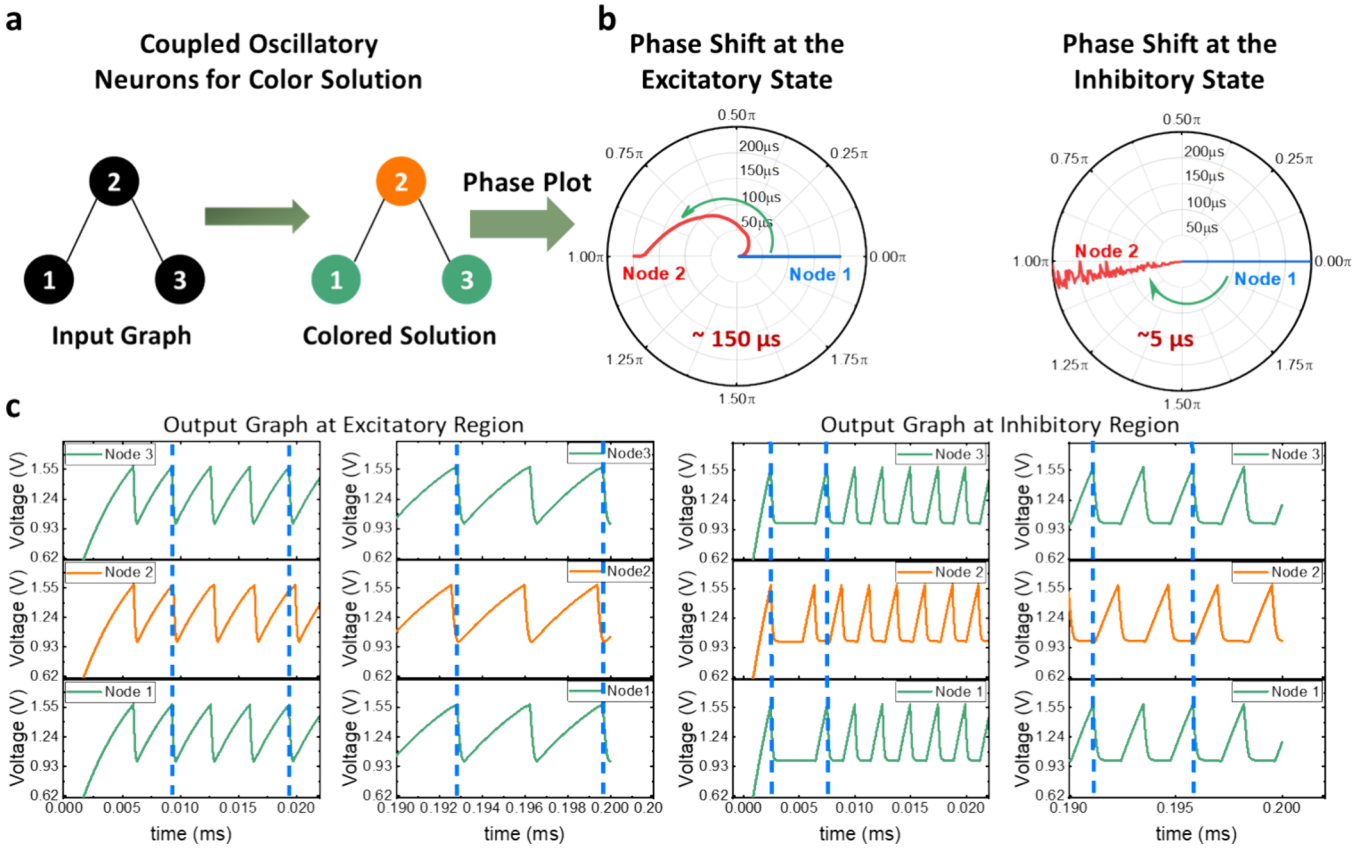


Figure 7. Simulated vertex coloring using an OTS-based oscillatory neural network. (a) Circuit schematic of a simulated three-node network composed of coupled OTS neurons, with R_{int} = 2.5 kΩ, R_{ext} = 47 kΩ, C_p = 117 pF, and coupling capacitance C_c = 2 pF between connected nodes, where Node 2 is connected to Nodes 1 and 3, while Nodes 1 and 3 are not directly connected. The coupled capacitors introduce phase-repulsive interactions between connected nodes, leading to phase separation and enabling vertex coloring. (b) Polar representation of the phase evolution under excitatory and inhibitory operating regimes. Node 1 is selected as the phase reference, and the maximum time delay is defined as 180°. In the excitatory regime, the phase trajectory gradually evolves and reaches a stable state after approximately 150 µs. In the inhibitory regime, the phase trajectory evolves in the opposite direction and converges within approximately 5 µs, indicating faster stabilization of the coloring solution. (c) Time-domain voltage waveforms of the coupled neurons, showing the evolution of spike timing and phase relationships. In the excitatory regime, Node 2 lags behind Node 1, whereas in the inhibitory regime, Node 2 leads Node 1. After convergence, the relative spike timing between nodes remains constant, indicating a stable phase-separated coloring state.

connected neurons progressively separate in phase due to the phase-repulsive capacitive interactions, whereas neurons without direct edge connections tend to maintain phase-adjacent states because of the weak phase constraint, thereby forming synchronized clusters. After stabilization, the three-node network converges into two distinct phase states (two colors), where Nodes 1 and 3 share a similar phase, while Node 2 occupies a separate phase state, as illustrated in the right panel of Figure 7a. This spontaneous phase clustering effectively maps the vertex-coloring solution into the phase domain through the intrinsic synchronization dynamics of the coupled OTS neurons.

Importantly, the role of excitatory-inhibitory dynamics extends beyond simply enabling oscillations; it directly governs how phase relationships evolve and stabilize. In the excitatory regime, the coupling between neurons is less efficient; thus, the network needs more time to separate the phases. In contrast, in the inhibitory regime, enhanced filament retention modifies the discharge dynamics, leading to a shift in spike timing and a reordering of phase relationships. The phase evolution under different operating regimes is shown in Figure 7b, where the red and blue curves represent the phase trajectories of Nodes 2 and 1, respectively. Initially, all neurons exhibit nearly identical oscillatory behavior, resulting in overlapping phase states corresponding to the same color. As the coupled dynamics evolve, the phase of Node 2 progressively separates from Node 1 due to the capacitive phase-repulsive interactions. After stabilization, the phase difference between Nodes 1 and 2 converges to approximately 180°, corresponding to two distinct phase states (two colors). Although both regimes eventually reach the same stable coloring solution, the phase trajectory of Node 2 evolves differently in each case, reflecting distinct synchronization pathways and convergence dynamics. As the coupled dynamics evolve, the capacitive interactions force connected neurons to separate in spike timing, leading to divergence in their phase trajectories. With further evolution, the relative delay between neighboring neurons gradually converges to a constant value. A stable solution is therefore defined when the phase difference between all connected nodes no longer changes with time and remains constant over consecutive oscillation cycles. In this work, Node 1 is selected as the phase reference, and the maximum delay between neurons is defined as 180°. The phase trace is calculated from the spike-time shift

https://doi.org/10.1021/acsami.6c15034
ACS Appl. Mater. Interfaces 2026, 18, 59518−59533

Downloaded from pubs.acs.org/aamick/article-pdf/18/43/59518/6897174/am-2026-15034u.pdf by LIVERPOOL JOHN MOORES UNIV user on 05 November 2026

relative to Node 1. When the neuron operates in the excitatory regime, the phase trajectory of Node 2 increases counterclockwise and gradually approaches a constant angular separation. The phase evolution becomes stable after approximately 150 μs, indicating that the relative spike delays between nodes have reached fixed values and the coloring solution has converged. In contrast, when the neuron operates in the inhibitory regime, the phase trajectory evolves in the opposite direction and reaches a stable phase distribution after only approximately 5 μs. Additional simulations performed over a wider range of operating biases show an overall decrease in convergence time with increasing bias, as shown in Figure S23. The faster convergence in the inhibitory regime originates from the prolonged ON-state retention of the OTS at higher bias. Once the device switches ON, the longer conductive duration allows the capacitively coupled neurons to interact for a longer period during each oscillation cycle, thereby enhancing the coupling interaction and accelerating phase separation. Thus, under the present network conditions, the inhibitory regime provides substantially faster convergence than the excitatory regime. Once the trajectories reach their steady-state values, the angular separation between connected nodes remains nearly unchanged, confirming that the network has reached a stable coloring solution. This difference is further evident in the time-domain responses shown in Figure 7c, where the relative spike timing between nodes reverses depending on the operating regime. For example, Node 2 lags behind Node 1 in the excitatory regime, while it leads in the inhibitory regime, despite identical network topology and operating frequency. To further examine the robustness of this phase-convergence behavior in the high-bias regime, the effect of stochastic filament rupture was separately examined using a time-dependent dielectric breakdown (TDDB)-like stochastic model in LTspice. The resulting phase evolution shows similar phase-separation behavior (Figure S24), indicating that the network convergence is preserved in the presence of stochastic filament rupture. In addition, the sensitivity of phase convergence to device-to-device variation in threshold voltage was evaluated by assigning V_{th} = 1.46, 1.54, and 1.62 V to Nodes 1, 2, and 3, respectively. In the excitatory regime, the network does not converge to the intended phase configuration under the investigated conditions because the V_{th} mismatch perturbs the individual oscillation timing. Such mismatch could potentially be mitigated through voltage calibration or other compensation approaches.[56−58] In the self-inhibitory regime, stable convergence can be recovered by increasing the coupling capacitance. As shown in Figure S25, with C_c = 2 pF, the phases do not reach the intended stable configuration, whereas increasing C_c to 10 pF results in rapid convergence. The prolonged conductive duration in the self-inhibitory regime increases the interaction time between coupled neurons, while the larger coupling capacitance strengthens the phase-repulsive interaction and helps compensate for the phase detuning caused by D2D variability. This highlights that the excitatory-inhibitory balance provides an additional degree of freedom for tuning the dynamical evolution, convergence behavior, and robustness of the network without altering its structural connectivity.

3. CONCLUSIONS

We proposed a GeAsTe-based OTS neuron capable of exhibiting non-monotonic excitatory-inhibitory spiking behavior using only a simple resistor-capacitor circuit. The firing frequency initially increases with input intensity and then decreases beyond the inflection voltage point because of the competition between RC charging dynamics and conductive filament retention. Unlike the previously reported time-dependent SFA and stochastic firing dynamics in OTS neurons,[32] the present work demonstrates a bias-dependent non-monotonic frequency response governed by the applied voltage and filament-retention dynamics. To understand and predict the neuron behavior, we use several complementary models: one based on filament, electron tunneling, and heat dynamics, the threshold-voltage model; and a physics-informed compact model based on defect-state transitions for filament evolution. These complementary models successfully reproduce the complex spiking dynamics, dynamical bifurcations, threshold voltage, holding voltage, and switching behavior of the OTS device over a wide range of temperatures (77−293 K) and internal resistances (600 Ω−38 kΩ). In addition, the models accurately capture the excitatory-inhibitory spiking dynamics and transition, as well as clarify the mechanisms of observed phenomena and the influence of external circuit parameters. Increasing R_{ext} or decreasing R_{int} shifts the inflection voltage point toward higher bias, whereas increasing C_{ext} reduces the maximum oscillation frequency without changing the underlying non-monotonic behavior. Finally, a coupled oscillatory OTS neuron network was demonstrated through circuit simulations for solving a vertex coloring problem within 5 μs, highlighting the strong potential of OTS-based neurons for compact and energy-efficient brain-inspired computing, while the proposed models provide a useful framework for accelerating future device-circuit co-design and extending their other OTS functionalities such as relaxation and selector-only memory.

4. EXPERIMENTAL SECTION

4.1. Electrical Measurement of OTS Devices and Artificial Neuron Circuits

Electrical characterization of both the standalone OTS devices and the artificial neuron circuits was performed using a Keithley 4200A-SCS Parameter Analyzer. DC current-voltage characteristics were measured using the embedded SMU module combined with a preamplifier to improve low-current resolution and measurement precision. The switching dynamics, oscillatory neuron behavior, and pulse responses were characterized using the embedded 4225-PMU ultrafast pulse module. Both the SMU and PMU modules were connected through remote performance modules (RPMs) to reduce parasitic effects and measurement noise. Two independent RPM channels were used for the two-terminal OTS device measurements. The external resistor and capacitor used in the neuron circuit were mounted on a printed circuit board (PCB) and connected through terminal blocks to allow stable electrical contact and easy replacement of circuit components. The OTS devices were connected to the measurement system using coaxial cables and probe needles through a probe station setup. In addition, the switching speed of the OTS device was measured using an ultrafast arbitrary waveform generator (Active Technologies AWG7202, 10 GHz) together with a high-speed oscilloscope (Keysight Technologies DSAV084A, 8 GHz).

4.2. Dynamical Model for Spiking Simulations/Method

To simulate the excitation and inhibition dynamics of an artificial neuron, we employ a model involving three key elements: (i) diffusion of conductive nanoclusters through the dielectric matrix of a memristor, with resistance switching controlled by filament dynamics; (ii)

Downloaded from pubs.acs.org/aamick/article-pdf/18/43/59518/6897174/am-2026-15034u.pdf by LIVERPOOL JOHN MOORES UNIV user on 05 November 2026

https://doi.org/10.1021/acsami.6c15034
ACS Appl. Mater. Interfaces 2026, 18, 59518−59533

tunnelling of electrons between the terminals along filaments through nanoclusters; and (iii) thermal dynamics controlled by Joule heating and heat dissipation through the device substrate.[59−62] The stochastic model[59−62] has been shown to describe the experimental findings well.[26,59−61,63] To make the simulations more tractable, it is convenient to reduce the dynamics of the whole filament to the simulation of a single conductive cluster in the filament bottleneck that determines resistance switching.[26,62−64] In this approximation, the model can be reduced to a set of three stochastic differential equations,[26] which successfully predict the properties of an artificial neuron. However, this model still obscures the deterministic dynamics of artificial-neuron spiking because of thermal fluctuations, which change in intensity as the conductive cluster diffuses. To retain the essential heat dynamics while eliminating noisy fluctuations, we omit random forces in the cluster dynamics and add deterministic forces associated with thermophoretic and/or thermoelectric effects.[65,66] As a result, we derive a set of equations describing the cluster position x, the voltage V across the memristor, the temperature gradient T' that determines the additional force acting on the cluster, and the electric gradient V' in the memristor, all as functions of time t:

$$\eta \frac{dx}{dt} = -\frac{\partial U}{\partial x} - q\frac{V}{L} - q_T T' \tag{1a}$$

$$\frac{dT'}{dt} = \frac{2VV'R - V^2R'}{C_{th}[R(x)]^2} - \kappa T' \tag{1b}$$

$$\tau \frac{dV}{dt} = V_{ext} - \left(1 + \frac{R_{ext}}{R(x)}\right)V \tag{1c}$$

$$\tau \frac{dV'}{dt} = -\left(1 + \frac{R_{ext}}{R(x)}\right)V' + \frac{R_{ext}R'}{[R(x)]^2}V \tag{1d}$$

$$R(x) = R_0 \cosh\left(\frac{x}{\lambda}\right) \tag{1e}$$

where the cluster dynamics are governed by an overdamped equation with viscosity η, phenomenological electrochemical potential U, electric charge q, and thermal charge q_T, determined by the thermophoresis and/or Seebeck coefficients. The equation for the thermal gradient is obtained from Newton's cooling law, with heat capacitance C_{th} and thermal conductance κ to the substrate. The third equation follows from Kirchhoff's laws for the circuit, with RC time constant τ and external load resistance R_{ext} of the artificial neuron. This Kirchhoff equation also determines the equation for the electric gradient (the fourth equation in the set). Electrons hop to the cluster from the filament and to the memristor terminal, which determines the tunnelling equation (the fifth equation), with minimum memristor resistance R_0 and tunnelling length λ. These five equations can be written in dimensional form and integrated numerically (see the Supplementary Materials in ref. 26) for the potential shown in the inset of Figure S26.

4.3. Circuit Simulation of the Coupled OTS Neuron Network

The three-node OTS neuron network was simulated in LTspice using the compact OTS model. Each neuron was implemented with R_{int} = 2.5 kΩ, R_{ext} = 47 kΩ, and C_p = 117 pF. Connected neurons were coupled through C_c = 2 pF capacitors to generate phase-repulsive interactions. For the simulations presented, the filament-retention behavior was represented using the average retention time. Additional simulations incorporating stochastic filament rupture were performed using a time-dependent dielectric breakdown (TDDB)-like sampling approach to evaluate the robustness of the phase-separation behavior. The phase of each neuron was calculated directly from its spike timing. The spike times of all three nodes were extracted from their simulated voltage waveforms, with Node 1 selected as the phase reference. For the kth oscillation cycle, the period of Node 1 was calculated from two consecutive spikes as $T_1,k = t_1,k+1 - t_1,k$. The relative time delay of Node i with respect to Node 1 was defined as $\Delta t_i k = t_i k - t_1,k$, and the corresponding relative delay was calculated as $d_i k = \Delta t_i k / T_1,k$. The maximum delay between nodes is defined as Δd. Here, the relative phase was calculated as $\varphi_i k = \pi d_i k / \Delta d$. Phase locking was identified when the relative phase difference between the coupled neurons remained approximately constant over successive oscillation cycles. Continuous oscillation of all coupled neurons was additionally verified from their time-domain voltage waveforms. As shown in Figure S27, all three nodes continue to undergo repeated switching in the inhibitory regime without becoming permanently trapped in either the ON or OFF state. Following convergence, Nodes 1 and 3 exhibit approximately the same phase, whereas Node 2 maintains a separated phase state. This confirms that the phase separation used for vertex coloring arises from sustained oscillatory dynamics rather than temporary or permanent quenching of individual neurons.

■ ASSOCIATED CONTENT

Supporting Information

The Supporting Information is available free of charge at https://pubs.acs.org/doi/10.1021/acsami.6c15034.

Schematic illustration of the GeAsTe-based Ovonic threshold switching (OTS) device structure, transient switching response, and DC current−voltage characteristics; statistical distributions of the threshold and holding voltages over 2000 switching cycles; ultrafast transient switching dynamics of the OTS device; frequency-extraction waveform with different ramp rate; Bias-dependent spike waveforms illustrating the excitatory- and inhibitory-like regimes and cycle-to-cycle/device-to-device frequency reproducibility; temperature and internal-resistance dependence of the threshold and holding voltages; compact-model parameter-sensitivity analysis; period-jitter and mean-versus-median ISI analysis; Statistical analysis of charging time, discharging time, retention time and holding-time distributions under different bias conditions; and evolution of the characteristic charging and holding time constants; Simulated spike waveforms predicted by the dynamical model, bias-dependent balance between charging and ON-state retention, energy consumption per spike and comparison with representative artificial spiking neurons; effects of external resistance, external capacitance, and internal resistance on charging and holding dynamics; normalized frequency−voltage characteristics under varying circuit parameters; device-to-device circuit-parameter measurements; bias-dependent network convergence, and the impacts of stochastic filament rupture and D2D variability on the convergency; the electrochemical-potential profile used in deterministic spiking simulations of the OTS artificial neuron; and time-domain verification of sustained oscillation and phase separation in the coupled OTS neuron network (DOCX)

■ AUTHOR INFORMATION

Corresponding Authors

Weidong Zhang − *School of Engineering, Liverpool John Moores University, Liverpool L3 3AF, U.K.;* orcid.org/0000-0003-4600-7382; Email: W.Zhang@ljmu.ac.uk

https://doi.org/10.1021/acsami.6c15034
ACS Appl. Mater. Interfaces 2026, 18, 59518−59533

Downloaded from pubs.acs.org/aamick/article-pdf/18/43/59518/6897174/am-2026-15034u.pdf by LIVERPOOL JOHN MOORES UNIV user on 05 November 2026

Muhammad Naqi − *School of Engineering, Liverpool John Moores University, Liverpool L3 3AF, U.K.;* orcid.org/0000-0002-1549-4379; Email: m.naqi@ljmu.ac.uk

Authors

Guosheng Wang − *School of Engineering, Liverpool John Moores University, Liverpool L3 3AF, U.K.*

Zeyu Hu − *School of Engineering, Liverpool John Moores University, Liverpool L3 3AF, U.K.*

Chengcheng Wang − *School of Engineering, Liverpool John Moores University, Liverpool L3 3AF, U.K.*

Nishant Saxena − *School of Engineering, Liverpool John Moores University, Liverpool L3 3AF, U.K.*

Linxi Zhang − *School of Engineering, Liverpool John Moores University, Liverpool L3 3AF, U.K.*

Zheng Chai − *Center for Spintronics and Quantum Systems, The School of Materials Science and Engineering, Xi'an Jiaotong University, Xi'an 710049, China*

Sergey Savel'ev − *Department of Physics, Loughborough University, Loughborough LE11 3TU, U.K.*

Alexander Balanov − *Department of Physics, Loughborough University, Loughborough LE11 3TU, U.K.*

Pavel Borisov − *Department of Physics, Loughborough University, Loughborough LE11 3TU, U.K.*

Fariba Sharifian − *School of Computer Science and Mathematics, Liverpool John Moores University, Liverpool L3 3AF, U.K.*

Complete contact information is available at: https://pubs.acs.org/doi/10.1021/acsami.6c15034

Author Contributions

[†]G.W. and Z.H. contributed equally to this work. W.Z. and M.N. conceived and supervised the project. G.W. and Z.H. designed and simulated the compact model, performed the experiments, and conducted the electrical measurements. G.W. and M.N. analyzed the data and prepared the initial manuscript. C.W., N.S., L.Z., and Z.C. contributed to experimental data analysis. S.S., A.B., and P.B. performed the dynamical modelling and simulations. F.S. contributed to data analysis and interpretation. W.Z., M.N., and Z.C. directed the research and revised the manuscript. All authors wrote and contributed to the manuscript.

Notes

The authors declare no competing financial interest.

■ ACKNOWLEDGMENTS

This work is supported in part by the EPSRC of the UK under Grants EP/Y008235/1 and EP/Z536180/1. The authors gratefully acknowledge their colleagues at IMEC for preparing and providing the OTS devices, as well as for their valuable technical guidance.

■ REFERENCES

(1) Gao, Q.; Meng, H.; Wu, E.; Zhuang, X.; Li, Y. A Flexible, Broadband Optoelectronic Memristor for Neuromorphic Visual Perception and Intelligent Image Processing. *Adv. Func. Mater.* **2026**, *36* (19), e20981.

(2) Chen, X.; Yang, D.; Hwang, G.; Dong, Y.; Cui, B.; Wang, D.; Chen, H.; Lin, N.; Zhang, W.; Li, H.; et al. Oscillatory Neural Network-Based Ising Machine Using 2D Memristors. *ACS Nano* **2024**, *18* (16), 10758−10767.

(3) Wang, Y.; Gong, Y.; Huang, S.; Xing, X.; Lv, Z.; Wang, J.; Yang, J.-Q.; Zhang, G.; Zhou, Y.; Han, S.-T. Memristor-based biomimetic compound eye for real-time collision detection. *Nat. Commun.* **2021**, *12* (1), 5979.

(4) Wong, H. S. P.; Salahuddin, S. Memory leads the way to better computing. *Nat. Nanotechnol.* **2015**, *10* (3), 191−194.

(5) Ambrogio, S.; Narayanan, P.; Tsai, H.; Shelby, R. M.; Boybat, I.; di Nolfo, C.; Sidler, S.; Giordano, M.; Bodini, M.; Farinha, N. C. P.; et al. Equivalent-accuracy accelerated neural-network training using analogue memory. *Nature* **2018**, *558* (7708), 60−67.

(6) Sugie, T.; Akamatsu, T.; Nishitsuji, T.; Hirayama, R.; Masuda, N.; Nakayama, H.; Ichihashi, Y.; Shiraki, A.; Oikawa, M.; Takada, N.; et al. High-performance parallel computing for next-generation holographic imaging. *Nat. Electron.* **2018**, *1* (4), 254−259.

(7) Pei, J.; Deng, L.; Song, S.; Zhao, M.; Zhang, Y.; Wu, S.; Wang, G.; Zou, Z.; Wu, Z.; He, W.; et al. Towards artificial general intelligence with hybrid Tianjic chip architecture. *Nature* **2019**, *572* (7767), 106−111.

(8) Roy, K.; Jaiswal, A.; Panda, P. Towards spike-based machine intelligence with neuromorphic computing. *Nature* **2019**, *575* (7784), 607−617.

(9) Merolla, P. A.; Arthur, J. V.; Alvarez-Icaza, R.; Cassidy, A. S.; Sawada, J.; Akopyan, F.; Jackson, B. L.; Imam, N.; Guo, C.; Nakamura, Y.; et al. A million spiking-neuron integrated circuit with a scalable communication network and interface. *Science* **2014**, *345* (6197), 668−673.

(10) Davies, M.; Srinivasa, N.; Lin, T. H.; Chinya, G.; Cao, Y.; Choday, S. H.; Dimou, G.; Joshi, P.; Imam, N.; Jain, S.; et al. Loihi: A Neuromorphic Manycore Processor with On-Chip Learning. *IEEE Micro* **2018**, *38* (1), 82−99.

(11) Frenkel, C.; Lefebvre, M.; Legat, J. D.; Bol, D. A 0.086-mm$\hat{}$2$ 12.7-pJ/SOP 64k-Synapse 256-Neuron Online-Learning Digital Spiking Neuromorphic Processor in 28-nm CMOS. *IEEE Trans. Biomed. Circuits Syst.* **2019**, *13* (1), 145−158.

(12) Indiveri, G.; Chicca, E.; Douglas, R. A VLSI array of low-power spiking neurons and bistable synapses with spike-timing dependent plasticity. *IEEE Trans. Neural Netw.* **2006**, *17* (1), 211−221.

(13) Han, J.-K.; Yun, S.-Y.; Lee, S.-W.; Yu, J.-M.; Choi, Y.-K. A Review of Artificial Spiking Neuron Devices for Neural Processing and Sensing. *Adv. Func. Mater.* **2022**, *32* (33), 2204102.

(14) Lim, D.-H.; Wu, S.; Zhao, R.; Lee, J.-H.; Jeong, H.; Shi, L. Spontaneous sparse learning for PCM-based memristor neural networks. *Nat. Commun.* **2021**, *12* (1), 319.

(15) Nandakumar, S. R.; Le Gallo, M.; Boybat, I.; Rajendran, B.; Sebastian, A.; Eleftheriou, E. A phase-change memory model for neuromorphic computing. *J. Appl. Phys.* **2018**, *124* (15), 152135.

(16) Bhatnagar, V.; Kumar, A. A Comprehensive Review of Phase Change Memory for Neuromorphic Computing: Advancements, Challenges, and Future Directions. *Energy Storage* **2025**, *7* (7), e70272.

(17) Yoon, J. H.; Song, Y.-W.; Ham, W.; Park, J.-M.; Kwon, J.-Y. A review on device requirements of resistive random access memory (RRAM)-based neuromorphic computing. *APL Mater.* **2023**, *11* (9), 090701.

(18) Dong, Z.; Zhou, Z.; Li, Z.; Liu, C.; Huang, P.; Liu, L.; Liu, X.; Kang, J. Convolutional Neural Networks Based on RRAM Devices for Image Recognition and Online Learning Tasks. *IEEE Trans. Electron Devices* **2019**, *66* (1), 793−801.

(19) Li, Y.; Chen, J.; Wang, L.; Zhang, W.; Guo, Z.; Wang, J.; Han, Y.; Li, Z.; Wang, F.; Dou, C.; et al. An ADC-Less RRAM-Based Computing-in-Memory Macro With Binary CNN for Efficient Edge AI. *IEEE Trans. Circuits Syst. II Express Briefs* **2023**, *70* (6), 1871−1875.

(20) Ban, S.; Lee, J.; Seo, Y.; Lee, W.; Kim, T.; Hwang, H. Advances in Ovonic Threshold Switch Selector Technologies for Storage Class Memory: From Fundamentals to Development and Beyond. *Adv. Electron. Mater.* **2025**, *11* (6), 2400665.

(21) Byun, U.; Na, H.; Kim, S. Universal Neuromorphic Element: NbO_x Memristor with Co-Existing Volatile, Non-Volatile, and Threshold Switching. *Adv. Func. Mater.* **2026**, *36* (15), e19431.

Downloaded from pubs.acs.org/aamick/article-pdf/18/43/59518/6897174/am-2026-15034u.pdf by LIVERPOOL JOHN MOORES UNIV user on 05 November 2026

(22) Zhang, X.; Zhuo, Y.; Luo, Q.; Wu, Z.; Midya, R.; Wang, Z.; Song, W.; Wang, R.; Upadhyay, N. K.; Fang, Y.; et al. An artificial spiking afferent nerve based on Mott memristors for neurorobotics. *Nat. Commun.* **2020**, *11* (1), 51.
(23) Yang, K.; Wang, Y.; Tiw, P. J.; Wang, C.; Zou, X.; Yuan, R.; Liu, C.; Li, G.; Ge, C.; Wu, S.; et al. High-order sensory processing nanocircuit based on coupled VO_2 oscillators. *Nat. Commun.* **2024**, *15* (1), 1693.
(24) Ju, D.; Kim, S. Versatile NbO_x-Based Volatile Memristor for Artificial Intelligent Applications. *Adv. Func. Mater.* **2024**, *34* (49), 2409436.
(25) Fu, Y.; Zhou, Y.; Huang, X.; Dong, B.; Zhuge, F.; Li, Y.; He, Y.; Chai, Y.; Miao, X. Reconfigurable Synaptic and Neuronal Functions in a $V/VO_x/HfWO_x/Pt$ Memristor for Nonpolar Spiking Convolutional Neural Network. *Adv. Func. Mater.* **2022**, *32* (23), 2111996.
(26) Midya, R.; Pawar, A. S.; Pattnaik, D. P.; Mooshagian, E.; Borisov, P.; Albright, T. D.; Snyder, L. H.; Williams, R. S.; Yang, J. J.; Balanov, A. G.; et al. Artificial transneurons emulate neuronal activity in different areas of brain cortex. *Nat. Commun.* **2025**, *16* (1), 7289.
(27) Zhao, R.; Wang, T.; Moon, T.; Xu, Y.; Zhao, J.; Sud, P.; Kim, S. J.; Liao, H.-T.; Zhuo, Y.; Midya, R.; et al. A spiking artificial neuron based on one diffusive memristor, one transistor and one resistor. *Nat. Electron.* **2025**, *8* (12), 1211−1221.
(28) Zhao, Z.; Clima, S.; Garbin, D.; Degraeve, R.; Pourtois, G.; Song, Z.; Zhu, M. Chalcogenide Ovonic Threshold Switching Selector. *Nano-Micro Lett.* **2024**, *16* (1), 81.
(29) Hu, Z.; Wang, G.; Chai, Z.; Zhang, W.; Garbin, D.; Degraeve, R.; Clima, S.; Ravsher, T.; Fantini, A.; Zhang, J. F.; et al. Understanding the Variability in GeAsTe Ovonic Threshold Switching Devices. In *2024 IEEE International Electron Devices Meeting (IEDM)*, 7-11 Dec. 2024, **2024**; pp 1−4.
(30) Hu, Z.; Zhang, W.; Degraeve, R.; Garbin, D.; Chai, Z.; Saxena, N.; Freitas, P.; Fantini, A.; Ravsher, T.; Clima, S.; et al. New Insights of the Switching Process in GeAsTe Ovonic Threshold Switching (OTS) Selectors. *IEEE Trans. Electron Devices* **2023**, *70* (2), 812−818.
(31) Lee, J.; Kim, S.; Park, S.; Lee, J.; Hwang, W.; Cho, S. W.; Lee, K.; Kim, S. M.; Seong, T.-Y.; Park, C.; et al. An Artificial Tactile Neuron Enabling Spiking Representation of Stiffness and Disease Diagnosis. *Adv. Mater.* **2022**, *34* (24), 2201608.
(32) Lee, M.; Cho, S. W.; Kim, S. J.; Kwak, J. Y.; Ju, H.; Yi, Y.; Cheong, B.-K.; Lee, S. Simple Artificial Neuron Using an Ovonic Threshold Switch Featuring Spike-Frequency Adaptation and Chaotic Activity. *Phys. Rev. Appl.* **2020**, *13* (6), 064056.
(33) Im, S.; Hwang, J.; Jeong, J.-S.; Lee, H.; Park, M. H.; Cho, J. H.; Ju, H.; Lee, S. Stochastic artificial neuron based on Ovonic Threshold Switch (OTS) and its applications for Restricted Boltzmann Machine (RBM). *Chaos, Solitons Fractals* **2024**, *186*, 115195.
(34) Pang, Y.; Zhou, Y.; Qiu, S.; Tong, L.; Zhao, N.; Xu, J.-B. Artificial non-monotonic neurons based on nonvolatile anti-ambipolar transistors. *Nat. Commun.* **2025**, *16* (1), 3188.
(35) Zhang, Y. V.; Ni, J.; Montell, C. The Molecular Basis for Attractive Salt-Taste Coding in Drosophila. *Science* **2013**, *340* (6138), 1334−1338.
(36) Gepshtein, S.; Pawar, A. S.; Kwon, S.; Savel'ev, S.; Albright, T. D. Spatially distributed computation in cortical circuits. *Sci. Adv.* **2022**, *8* (16), eabl5865.
(37) Weiher, M.; Herzig, M.; Tetzlaff, R.; Ascoli, A.; Mikolajick, T.; Slesazeck, S. Improved Vertex Coloring With NbO Memristor-Based Oscillatory Networks. *IEEE Trans. Circuits Syst. I Regul. Pap.* **2021**, *68* (5), 2082−2095.
(38) Li, Z.; Tang, W.; Zhang, B.; Yang, R.; Miao, X. Emerging memristive neurons for neuromorphic computing and sensing. *Sci. Technol. Adv. Mater.* **2023**, *24* (1), 2188878.
(39) Abed Zadeh, A.; Turner, B. D.; Calakos, N.; Brunel, N. Non-monotonic effects of GABAergic synaptic inputs on neuronal firing. *PLoS Comput. Biol.* **2022**, *18* (6), e1010226.
(40) Wu, G. K.; Li, P.; Tao, H. W.; Zhang, L. I. Nonmonotonic Synaptic Excitation and Imbalanced Inhibition Underlying Cortical Intensity Tuning. *Neuron* **2006**, *52* (4), 705−715.
(41) Neugebauer, V.; Li, W. Processing of Nociceptive Mechanical and Thermal Information in Central Amygdala Neurons With Knee-Joint Input. *J. Neurophysiol.* **2002**, *87* (1), 103−112.
(42) Wilson, H. R.; Cowan, J. D. Excitatory and Inhibitory Interactions in Localized Populations of Model Neurons. *Biophys. J.* **1972**, *12* (1), 1−24.
(43) Cruddas, J.; Pang, J. C.; Fornito, A. Cortical traveling waves in time and space: Physics, physiology, and psychology. *Neuron* **2026**, *114* (6), 985−1005.
(44) Ermentrout, B. A.; Mahajan, A. R. Simulating, Analyzing, and Animating Dynamical Systems: A Guide to XPPAUT for Researchers and Students. *Appl. Mech. Rev.* **2003**, *56* (4), B53−B53.
(45) Doedel, E. J.; Champneys, A. R.; Dercole, F.; Fairgrieve, T. F.; Kuznetsov, Y. A.; Oldeman, B.; Paffenroth, R.; Sandstede, B.; Wang, X.; Zhang, C. *AUTO-07P: Continuation and bifurcation software for ordinary differential equations*, **2007**.
(46) Chawa, M. M. A.; Bedau, D.; Demirkol, A. S.; Reiner, J. W.; Stewart, D. A.; Grobis, M. K.; Tetzlaff, R. A Compact Model of Threshold Switching Devices for Efficient Circuit Simulations. *IEEE Trans. Circuits Syst. I Regul. Pap.* **2023**, *70* (11), 4530−4538.
(47) Fugazza, D.; Ielmini, D.; Lavizzari, S.; Lacaita, A. L. Distributed-Poole-Frenkel modeling of anomalous resistance scaling and fluctuations in phase-change memory (PCM) devices. In *2009 IEEE International Electron Devices Meeting (IEDM)*, 7-9 Dec., **2009**; pp 1−4.
(48) Degraeve, R.; Ravsher, T.; Kabuyanagi, S.; Fantini, A.; Clima, S.; Garbin, D.; Kar, G. S. Modeling and spectroscopy of ovonic threshold switching defects. In *2021 IEEE International Reliability Physics Symposium (IRPS)*, *21-25* March, **2021**; pp 1−5.
(49) Ravsher, T.; Degraeve, R.; Garbin, D.; Clima, S.; Fantini, A.; Donadio, G.; Kundu, S.; Devulder, W.; Hody, H.; Potoms, G.; et al. Comprehensive Performance and Reliability Assessment of Se-based Selector-Only Memory. In *2024 IEEE International Reliability Physics Symposium (IRPS)*, 14-18 April, **2024**; pp 7A.5-1−7A.5-9.
(50) Ravsher, T.; Degraeve, R.; Garbin, D.; Fantini, A.; Clima, S.; Donadio, G. L.; Kundu, S.; Hody, H.; Devulder, W.; Houdt, J. V.; et al. Polarity-dependent threshold voltage shift in ovonic threshold switches: Challenges and opportunities. In *2021 IEEE International Electron Devices Meeting (IEDM)*, 11-16 Dec., **2021**; pp 28.24.21−28.24.24.
(51) Chai, Z.; Zhang, W.; Degraeve, R.; Clima, S.; Hatem, F.; Zhang, J. F.; Freitas, P.; Marsland, J.; Fantini, A.; Garbin, D.; et al. Evidence of filamentary switching and relaxation mechanisms in GexSe1-xOTS selectors. In *2019 Symposium on VLSI Technology*, *9-14* June, **2019**; pp T238−T239.
(52) Zhang, W.; Chai, Z.; Freitas, P.; Zhang, J. F. Marsland, J. Relaxation in GeSe Ovonic Threshold Switching Device. In *2022 IEEE 16th International Conference on Solid-State & Integrated Circuit Technology (ICSICT)*, 25-28 Oct., **2022**; pp 1−4.
(53) Ascoli, A.; Weiher, M.; Tetzlaff, R.; Herzig, M.; Slesazeck, S.; Mikolajick, T. Control Strategies to Optimize Graph Coloring via M-CNNs with Locally-Active NbO_x Memristors. In *2021 10th International Conference on Modern Circuits and Systems Technologies (MOCAST)*, *5-7* July, **2021**; pp 1−8.
(54) Ascoli, A.; Weiher, M.; Herzig, M.; Slesazeck, S.; Mikolajick, T.; Tetzlaff, R. Graph Coloring via Locally-Active Memristor Oscillatory Networks. *J. Low Power Electron. Appl.* **2022**, *12*, 22.
(55) Raychowdhury, A.; Parihar, A.; Smith, G. H.; Narayanan, V.; Csaba, G.; Jerry, M.; Porod, W.; Datta, S. Computing With Networks of Oscillatory Dynamical Systems. *Proc. IEEE* **2019**, *107* (1), 73−89.
(56) Shamsi, J.; Avedillo, M. J.; Linares-Barranco, B.; Serrano-Gotarredona, T. Effect of Device Mismatches in Differential Oscillatory Neural Networks. *IEEE Trans. Circuits Syst. I Regul. Pap.* **2023**, *70* (2), 872−883.
(57) Graber, M.; Hofmann, K. An integrated coupled oscillator network to solve optimization problems. *Commun. Eng.* **2024**, *3* (1), 116.
(58) Dinç, N.; Sabo, F.; Todri-Sanial, A. Harnessing Phase Dynamics Across Diverse Frequencies with Multifrequency Oscillatory Neural Networks. *Adv. Intell. Discovery* **2025**, *2* (5), e202500152.

Downloaded from pubs.acs.org/aamick/article-pdf/18/43/59518/6897174/am-2026-15034u.pdf by LIVERPOOL JOHN MOORES UNIV user on 05 November 2026

https://doi.org/10.1021/acsami.6c15034
ACS Appl. Mater. Interfaces 2026, 18, 59518−59533

(59) Wang, Z.; Joshi, S.; Savel'ev, S. E.; Jiang, H.; Midya, R.; Lin, P.; Hu, M.; Ge, N.; Strachan, J. P.; Li, Z.; et al. Memristors with diffusive dynamics as synaptic emulators for neuromorphic computing. *Nat. Mater.* **2017**, *16* (1), 101−108.
(60) Jiang, H.; Belkin, D.; Savel'ev, S. E.; Lin, S.; Wang, Z.; Li, Y.; Joshi, S.; Midya, R.; Li, C.; Rao, M.; et al. A novel true random number generator based on a stochastic diffusive memristor. *Nat. Commun.* **2017**, *8* (1), 882.
(61) Wang, Z.; Joshi, S.; Savel'ev, S.; Song, W.; Midya, R.; Li, Y.; Rao, M.; Yan, P.; Asapu, S.; Zhuo, Y.; et al. Fully memristive neural networks for pattern classification with unsupervised learning. *Nat. Electron.* **2018**, *1* (2), 137−145.
(62) Savel'ev, S. E.; Marchesoni, F.; Bratkovsky, A. M. Mesoscopic resistive switch: non-volatility, hysteresis and negative differential resistance. *Eur. Phys. J. B* **2013**, *86* (12), 501.
(63) Pattnaik, D. P.; Ushakov, Y.; Zhou, Z.; Borisov, P.; Cropper, M. D.; Wijayantha, U. W.; Balanov, A. G.; Savel'ev, S. E. Temperature Control of Diffusive Memristor Hysteresis and Artificial Neuron Spiking. *Phys. Rev. Appl.* **2023**, *19* (2), 024065.
(64) Yi, W.; Savel'ev, S. E.; Medeiros-Ribeiro, G.; Miao, F.; Zhang, M. X.; Yang, J. J.; Bratkovsky, A. M.; Williams, R. S. Quantized conductance coincides with state instability and excess noise in tantalum oxide memristors. *Nat. Commun.* **2016**, *7* (1), 11142.
(65) Wang, M.; Bi, C.; Li, L.; Long, S.; Liu, Q.; Lv, H.; Lu, N.; Sun, P.; Liu, M. Thermoelectric Seebeck effect in oxide-based resistive switching memory. *Nat. Commun.* **2014**, *5* (1), 4598.
(66) Kumar, S.; Wang, Z.; Huang, X.; Kumari, N.; Davila, N.; Strachan, J. P.; Vine, D.; Kilcoyne, A. L. D.; Nishi, Y.; Williams, R. S. Conduction Channel Formation and Dissolution Due to Oxygen Thermophoresis/Diffusion in Hafnium Oxide Memristors. *ACS Nano* **2016**, *10* (12), 11205−11210.

Downloaded from pubs.acs.org/aamick/article-pdf/18/43/59518/6897174/am-2026-15034u.pdf by LIVERPOOL JOHN MOORES UNIV user on 05 November 2026

https://doi.org/10.1021/acsami.6c15034
ACS Appl. Mater. Interfaces 2026, 18, 59518−59533